UC Davis

UC Davis Previously Published Works

Title

Monitoring Protein—Protein Interactions in the Cyanobacterial Circadian Clock in Real Time via Electron Paramagnetic Resonance Spectroscopy

Permalink

https://escholarship.org/uc/item/7nc020vb

Journal

Biochemistry, 59(26)

ISSN

0006-2960

Authors

Chow, Gary K

Chavan, Archana G

Heisler, Joel C

et al.

Publication Date

2020-07-07

DOI

10.1021/acs.biochem.0c00279

Peer reviewed

eScholarship.org Powered by the California Digital Library
University of California

This is an open access article published under an ACS AuthorChoice License, which permits copying and redistribution of the article or any adaptations for non-commercial purposes.

Biochemistry

pubs.acs.org/biochemistry

From the Bench

Monitoring Protein−Protein Interactions in the Cyanobacterial Circadian Clock in Real Time via Electron Paramagnetic Resonance Spectroscopy

Gary K. Chow, Archana G. Chavan, Joel C. Heisler, Yong-Gang Chang, Andy LiWang,* and R. David Britt*

Cite This: *Biochemistry* 2020, 59, 2387−2400

Read Online

ACCESS | Metrics & More | Article Recommendations | Supporting Information

ABSTRACT: The cyanobacterial circadian clock in *Synechococcus elongatus* consists of three proteins, KaiA, KaiB, and KaiC. KaiA and KaiB rhythmically interact with KaiC to generate stable oscillations of KaiC phosphorylation with a period of 24 h. The observation of stable circadian oscillations when the three clock proteins are reconstituted and combined in vitro makes it an ideal system for understanding its underlying molecular mechanisms and circadian clocks in general. These oscillations were historically monitored in vitro by gel electrophoresis of reaction mixtures based on the differing electrophoretic mobilities between various phosphostates of KaiC. As the KaiC phospho-distribution represents only one facet of the oscillations, orthogonal tools are necessary to explore other interactions to generate a full description of the system. However, previous biochemical assays are discontinuous or qualitative. To circumvent these limitations, we developed a spin-labeled KaiB mutant that can differentiate KaiC-bound KaiB from free KaiB using continuous-wave electron paramagnetic resonance spectroscopy that is minimally sensitive to KaiA. Similar to wild-type (WT-KaiB), this labeled mutant, in combination with KaiA, sustains robust circadian rhythms of KaiC phosphorylation. This labeled mutant is hence a functional surrogate of WT-KaiB and thus participates in and reports on autonomous macroscopic circadian rhythms generated by mixtures that include KaiA, KaiC, and ATP. Quantitative kinetics could be extracted with improved precision and time resolution. We describe design principles, data analysis, and limitations of this quantitative binding assay and discuss future research necessary to overcome these challenges.

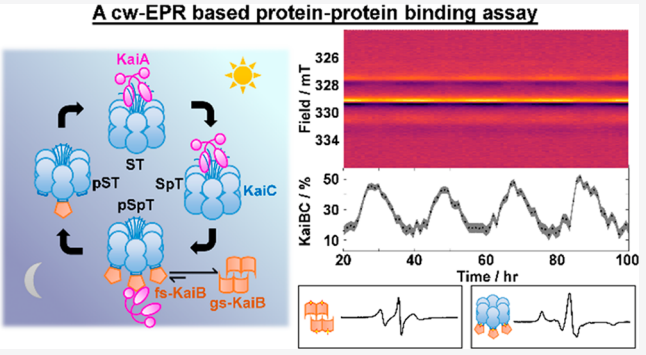

The circadian clock of the cyanobacterium *Synechococcus elongatus* regulates global gene expression[1] and provides a selective growth advantage.[2] The fact that transcriptional and translational oscillations (TTO) are unnecessary to drive posttranslational oscillations (PTOs)[3] sets this clock apart from circadian clocks from other organisms.[4] Indeed, in vitro reconstitution of the core oscillator proteins, KaiA, KaiB, and KaiC (Figure 1a), generates an autonomous macroscopic circadian rhythm of sequential KaiC phosphorylation−dephosphorylation at residues Ser-431 (S431) and Thr-432 (T432) in the presence of ATP[5,6] mirroring in vivo oscillations,[7] making the Kai system a unique model system for studying circadian clock systems in general.

KaiC belongs to the AAA+ ATPase family and consists of two homologous domains, CI and CII (Figure 1a).[8] CI possesses slow ATPase activity,[9−11] with its activity correlated with the frequencies of both TTO and PTO.[10] On the other hand, CII contains two phosphorylation sites, S431 and T432, that undergo ordered phosphorylation as S/T → S/pT → pS/pT → pS/T → S/T (p, phosphorylated).[5,6] This order is dictated by phosphorylation-dependent CII ring dynamics[12] and CI−CII ring stacking interactions.[13] The autophosphatase activity of CII is atypical in that ATP is regenerated from ADP and pS431 or pT432 as an intermediate prior to hydrolysis.[14]

In the absence of KaiA or KaiB, KaiC autophosphatase activity dominates, leading to an unphosphorylated $KaiC_{ST}$ resting state.[5] To drive autokinase activity in KaiC, KaiA, a domain-swapped homodimer (Figure 1a),[15] interacts with the C-terminal residues ("A-loops" and tail) of KaiC during the day (Figure 1a,b)[16,17] as a KaiAC complex. This KaiA−KaiC interaction promotes nucleotide exchange in KaiC and consequently autokinase activity in CII.[18,19] As CII progresses

Received: April 7, 2020
Revised: May 22, 2020
Published: May 26, 2020

Downloaded via UNIV OF CALIFORNIA MERCED on July 28, 2020 at 01:16:02 (UTC).
See https://pubs.acs.org/sharingguidelines for options on how to legitimately share published articles.

© 2020 American Chemical Society

https://dx.doi.org/10.1021/acs.biochem.0c00279
Biochemistry 2020, 59, 2387−2400

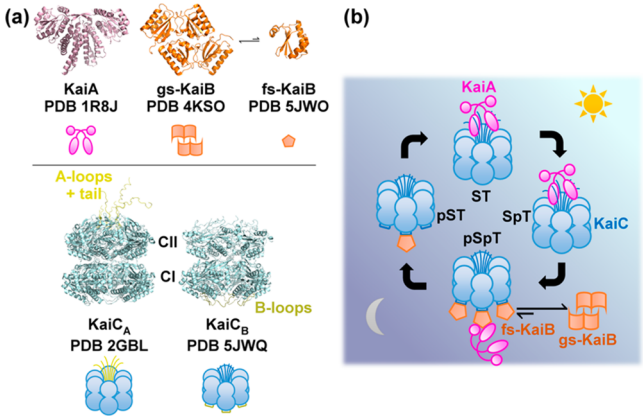

Figure 1. Overview of the core Kai oscillator. (a) Representative crystal structures and simplified representations of isolated clock components KaiA (magenta), KaiB [orange, ground state (gs) vs fold-switched (fs) states], and KaiC (blue, KaiA-binding competent state KaiC$_A$ vs KaiB-binding competent state KaiC$_B$). The crystal structure of KaiC$_B$ (Protein Data Bank entry 5JWQ) was obtained from the KaiC homologue in *Thermosynechococcus elongatus*. All other crystal structures were obtained from *S. elongatus*. For KaiC, the KaiA-binding A-loops and tail (yellow) and KaiB-binding B-loops (olive) are highlighted in both the crystal structures and simplified representations. (b) Model of events governing circadian oscillations in the Kai clock. Input and output pathways are not shown.

from S/T to pS/pT, corresponding to the day-to-night transition, the CII ring tightens, withdrawing its A-loops,[12] which decreases the binding affinity between KaiA and KaiC[20] and suppresses the autokinase activity in KaiC. This decrease in affinity is critical to maintaining macroscopic phase coherence.[20] Concurrently, the CII and CI rings of KaiC stack[13] such that CI adopts a posthydrolysis conformation that exposes its "B-loops" to KaiB binding (Figure 1b),[10,21] a step that marks the beginning of clock resetting.[22] The interchanging competences for KaiA and KaiB binding by two conformations of KaiC[23] are designated here as KaiC$_A$ and KaiC$_B$, respectively. Curiously, the conformation of KaiB that can bind to CI in this KaiBC complex differs from KaiB as crystallized in that the former has a thioredoxin fold and is termed fold-switched KaiB (fs-KaiB),[21,24] whereas the latter possesses an uncommon tetrameric state and is termed ground-state KaiB [gs-KaiB (Figure 1a)].[25,26] The tetramer and monomer have been shown to interconvert reversibly under native conditions,[27] whereas the mechanism of fold switching within monomerized KaiB remains elusive. On fold switching, a β-strand (β2) together with a newly formed α-helix (α3) in fs-KaiB is capable of KaiA binding, thereby stabilizing KaiA in an "autoinhibited" conformation where the CII-binding motif of KaiA is blocked.[21,28] The KaiB–KaiC$_{pS(p)T}$ binary complex can thus recruit KaiA to form a ternary KaiABC nighttime complex,[21,28] suppressing further KaiC phosphorylation and forming a negative feedback loop. Subsequent autodephosphorylation of KaiC$_{pS(p)T}$ during the night enables resetting of KaiC to KaiC$_{ST}$ and prepares the proteins for the next day. As the Kai system consists of discrete molecules, intrinsic stochastic noise can lead to desynchronization of the population.[29] To combat this, populations of KaiC synchronize via intersubunit allosteric interactions,[23,30] phosphorylation-dependent KaiA–KaiC binding affinities,[20,31] and monomer shuffling.[32,33]

Biochemical circadian rhythms of the Kai clock were first revealed by sodium dodecyl sulfate–polyacrylamide gel electrophoresis (SDS–PAGE) in which KaiC phosphostates in SDS-quenched reaction samples were quantitatively resolved.[5−7] As KaiC phosphodistribution represented only one facet of the Kai oscillator, coimmunoprecipitation assays[5,23] and native mass spectrometry[27] were developed in parallel in attempt to quantify relevant protein–protein interactions over the oscillations. However, the discontinuous nature of these assays meant that multiple samples had to be prepared to provide time-domain information. More recently, fluorescence correlation spectroscopy (FCS) and fluorescence polarization/anisotropy (FA) have been employed to study KaiB binding by fluorophore tagging, producing tagged proteins using either cell free synthesis[34,35] or site-directed mutagenesis.[24,36] Fluorescence assays are an improvement to previous discontinuous methods as the fluorescence signals could be continuously monitored provided the fluorophore tags are not photobleached. However, the myriad of stoichiometries existing in Kai reaction mixtures, tetrameric[26] and monomeric KaiB[24] and (sub)stoichiometric KaiBC and KaiABC complexes,[20,27,28] invalidate models that assume two species with differing molecular weights. Thus, fluorescence signals via either FCS or FA are not directly comparable to coimmunoprecipitation results, limiting their usefulness. Here, we introduce site-directed spin labeling–electron paramagnetic resonance (SDSL–EPR)[37] to probe real-time evolution of KaiB–KaiC interactions. SDSL–EPR provides an alternative to fluorescence assays by providing comparable time resolution while avoiding ambiguities in stoichiometry inherent to fluorescence-based methods. Furthermore, interaction specificity is maintained, allowing quantitative binding information comparable to coimmunoprecipitation or native-PAGE. In the following section, we discuss in detail the sample preparation and data analysis necessary to obtain reproducible results. Then, we describe the design principles to site-directed spin labeling. Once the theoretical background has been laid, we implement cw-EPR to the Kai system and demonstrate that cw-EPR gives complementary information to existing methods. Finally, we outline the limitations of this quantitative binding assay and discuss future research and instrumentation necessary to overcome these challenges.

MATERIALS AND METHODS

Cloning, Protein Expression, Purification, and Fluorescence/Spin Labeling. All genes were cloned into pET-28b using the NdeI/HindIII sites for production of SUMO fusion proteins. Details of the cloning protocol have been described previously.[12,13] Proteins were expressed in *Escherichia coli* BL21(DE3) (Novagen) and purified by Ni-NTA affinity chromatography and size-exclusion chromatography as described previously.[12,13] 6-Iodoacetamidofluorescein (6IAF) labeling of KaiB was performed according to a previous report.[24] A modified protocol for 3-iodoacetamido-PROXYL (3IAP) labeling of KaiB was performed as follows. A 5-fold excess of tris(2-carboxyethyl)phosphine (TCEP) was added to a purified aliquot of unlabeled KaiB (typically 100 μM) and incubated at room temperature for 15 min in labeling buffer [20 mM Tris and 150 mM NaCl (pH 8.0)], followed by overnight incubation of a 10-fold excess of 3IAP in the dark at 4 °C using a 200 mM 3IAP stock solution in DMSO. The difference in concentrations between the spin-label and TCEP is critical to a high labeling efficiency; TCEP is known to

https://dx.doi.org/10.1021/acs.biochem.0c00279
Biochemistry 2020, 59, 2387−2400

directly react with iodoacetamide-based fluorescent dyes[38] and is inferred to do the same to 3IAP, decreasing its effective concentration. After labeling, excess 3IAP was removed with a HiPrep 26/10 desalting column (GE Healthcare Life Sciences). The sample was then concentrated using Amicon ultrafiltration stirred cells fitted with 10 kDa cutoff membranes.

Protein Characterization. The concentrations of stock protein solutions were determined via a Bradford assay using bovine serum albumin (Thermo Fisher). All concentrations refer to the monomer unless otherwise stated. The labeling efficiencies of all spin-labeled KaiB samples were determined by electrospray ionization high-resolution liquid chromatography mass spectrometry [ESI-HR-LCMS (Figure S1)] using an LTQ Orbitrap XL mass spectrometer equipped with an electrospray ionization source (ThermoFisher, San Jose, CA) operating in positive ion mode. Fifty microliter portions of spin-labeled KaiB samples (400 μg/mL) were desalted using Zeba Spin Desalting Columns (ThermoFisher). LCMS was performed on a C18 column eluted with gradient of 0.1% formic acid in water to 0.1% formic acid in acetonitrile. The LCMS data were then analyzed using MagTran.[39] The labeling efficiency was determined by fitting the transformed spectrum with Gaussian lines and determining the peak areas of both labeled and unlabeled proteins. Samples that were not at least 95% labeled on the basis of LCMS peak areas were relabeled by repeating the labeling protocol described above.

Sample Preparations for In Vitro Kai Protein Reactions. All reactions were performed at 30 °C in reaction buffer [20 mM Tris, 150 mM NaCl (pH 8.0), 0.5 mM EDTA, 5 mM $MgCl_2$, and 1 mM ATP]. The in vitro 1× oscillator was carried out using 1.2 μM KaiA, 3.5 μM KaiB, and 3.5 μM KaiC. Fluorescence samples were prepared as 100 μL samples with additional 50 nM KaiB-K25C-6IAF included as described previously.[36] For real-time cw-EPR characterization, 10−40 μL samples were prepared by replacing WT-KaiB with spin-labeled KaiB. $KaiC_{S431E,T432E}$ ($KaiC_{EE}$) phosphomimetic reactions were performed with a 1× or 5× protein concentration without supplementing extra ATP. KaiB was added to $KaiC_{EE}$ and incubated for 7 h (5×) or 1 day (1×), after which KaiA was added to the KaiB/$KaiC_{EE}$ reaction mixture to a final Kai protein concentration of 4.6× (5×) or 0.9× (1×) relative to the 1× oscillator. Native-PAGE samples were prepared as 200 μL reaction mixtures at a 1× protein concentration and incubated at 30 °C overnight. Twenty microliters of the sample was then removed at predefined time points and mixed with 20 μL of 2× native-PAGE buffer [62.5 mM Tris, 20% (w/v) glycerol, 0.01% (w/v) bromophenol blue, 1 mM ATP, and 5 mM $MgCl_2$ (pH 6.8)] to give final KaiB and $KaiC_{EE}$ concentrations of 1.75 μM. The samples were frozen in a −80 °C freezer and then thawed over ice for 3 min prior to loading.

Native-PAGE. Thawed samples were electrophoresed at 60 V for 30 min followed by 140 V for 135 min using hand-cast 6% Tris-glycine mini gels with a 4% stacking gel in ATP-supplemented native-PAGE running buffer (25 mM Tris, 192 mM glycine, 1 mM ATP, and 5 mM $MgCl_2$) in an electrophoresis cell surrounded by ice−water. Gels were incubated in 0.5% SDS in 7.5% acetic acid, stained in SYPRO Orange (Fisher Scientific, Waltham, MA), and imaged using a BioSpectrum AC Imaging System (UVP, Upland, CA). Image contrast adjustment and densitometry were performed on ImageJ (National Institutes of Health). Formation of the KaiB−$KaiC_{EE}$ complex was estimated by normalizing the BC_{EE} complex band intensity against the sum of band intensities of the BC_{EE} complex and free $KaiC_{EE}$ (Figure S2).

Fluorescence Anisotropy (FA) Measurements. FA measurements of 1× oscillators (Figure S3) and phosphomimetic reactions (Figure S13) using 6IAF-labeled samples were performed at 30 °C on a BMG Clariostar plate reader (BMG LABTECH, Cary, NC) with an excitation wavelength of 492 nm and an emission wavelength of 530 nm.

EPR Spectroscopy. X-Band cw-EPR (9.2 GHz) spectra were recorded using a Bruker ECS 106 spectrometer equipped with an SHQE cavity. In vitro reaction spectra were recorded at 30 °C using 2 G modulation at a 100 kHz modulation frequency with a conversion time of 40 ms and a time constant of 20 ms. Scan times were approximately 7.5 min per spectrum. Samples were loaded into custom sample tubes by sealing one end of glass pipets (10 μL, Fisher Scientific) or rectangular miniature hollow tubing (20−40 μL, VitroCom, Mountain Lakes, NJ) to ensure a high quality factor (Q) and to suppress sample heating. For near-rigid limit samples for determination of g and A, the spin-labeled samples were mixed with WT-KaiB and equilibrated overnight followed by dilution to a final concentration of 17.5 μM labeled KaiB, 157.5 μM WT-KaiB, and 20% (w/w) sucrose (20 Bx), 100 μL (4 mm inside diameter, Wilmad, Vineland, NJ), and the spectra were recorded at −40 °C and 1 G modulation. Temperature control was achieved using an FTS XR401 Air-jet Crystal Cooler (SP Scientific, Stone Ridge, NY). Real-time temperature monitoring in the sample cavity was achieved using an external type T thermocouple (Omega Inc.) connected to a Universal Thermocouple Connector Direct USB to PC Connection (Omega Inc.) on a separate computer. The thermocouple readings inside the EPR sample tube and Air-jet outlet were consistent, ruling out microwave heating of the sample. The microwave frequency was continuously monitored externally via an EIP 578B frequency counter (National Instruments, Santa Clara, CA) connected to a separate computer.

EPR Data Preprocessing. Prior to data analysis, the EPR data were (1) microwave frequency drift corrected and (2) background subtracted as follows. Unlike previous spin labeling and spin trapping studies in which spectral acquisition is usually complete within hours, the Kai clock oscillates over a duration of days. The length of the acquisition process enables extensive averaging yet poses an additional challenge that the resonance microwave frequency of the resonance cavity can drift over time due to electronic imperfections, cavity and/or ambient-temperature changes, and sample evaporation. For a given spin system, this microwave frequency drift is manifested as a shift in the spectrum predicted by considering the Hamiltonian ($\hat{H}$).

$$\hat{H} = \mu_B B g \hat{S} + \hat{S} A \hat{I} + \ldots \leftrightarrow E = h\nu = \mu_B B g + A I + \ldots \tag{1a}$$

where μ_B is the Bohr magneton, B is the incident magnetic field, and g is the g factor. S and I are the electron and nuclear spin quantum numbers, respectively, and the energy states are coupled by an anisotropic hyperfine matrix A that is incompletely averaged by motion. For a single nitroxide component with an isotropic rotational correlation time (τ_c), a modest simulated frequency drift of 0.5 MHz over a 4 day period (Figure S4a) could lead to observable differences between the spectra at 0 h and 96 h (Figure S4b). Because similar levels of microwave frequency drift were observed in

https://dx.doi.org/10.1021/acs.biochem.0c00279
Biochemistry 2020, 59, 2387−2400

our experiments (Figure S4a), a correction (Figure S4c,d) was applied by either multiplying the magnetic field of each spectrum by the ratio of their microwave frequencies (eq 1b) or adding a linear term proportional to their frequency difference (eq 1c) followed by interpolation using MATLAB interpolation routine interp1:

$$B_1 = \frac{h\nu_1 - AI}{g\mu_B} + \ldots \approx \left(\frac{h\nu_0 - AI}{g\mu_B}\right)\left(\frac{\nu_1}{\nu_0}\right) + \ldots = \frac{B_0\nu_1}{\nu_0} \tag{1b}$$

$$B_1 = \frac{h\nu_1 - AI}{g\mu_B} = \frac{h\nu_1 - h\nu_0 + h\nu_0 - AI}{g\mu_B} = B_0 + \frac{h(\nu_1 - \nu_0)}{g\mu_B} \tag{1c}$$

Both correction schemes reduced the difference spectra to the noise level. The estimated error due to microwave frequency correction is 2 orders of magnitude smaller than the magnetic field intervals used (see the Supplementary Text for details). While microwave frequency correction is theoretically impossible as the Zeeman term of the spin Hamiltonian is linearly dependent on frequency whereas hyperfine is not and the g and A tensors are transition-dependent, with this difference forming the basis of multifrequency EPR,[40] we found this protocol to be a reasonable compromise to allow quantitative analysis over extended experimental durations.

To perform background subtraction, the background spectrum (B_{bg}) was first acquired using sample cells containing reaction buffer only. Then, the background spectrum was subtracted from the data (Figure S5). As the cw-EPR signal intensity is directly proportional to the resonator quality factor (Q),[41] intersample variations in Q could lead to variations in intensity in both the signal of interest originating from the spin-label and the resonator cavity background (Figure S5a,b). The signal intensity could also fluctuate due to microwave frequency detuning. Thus, the magnitude of background subtraction (w) applied was determined individually for each spectrum Y by considering only magnetic field positions that are not within the span of the nitroxide spectrum (null window, Figure S5b). This background subtraction is hence a linear regression problem to determine the weight of the background (w):

$$Y\ (\text{null window}) = (B_{bg}w_{bg})_{\text{null window}} \tag{2}$$

Once w is determined, the correction is applied to the entire spectrum to recover the background and baseline-corrected spectrum (Figure S5c).

Determination of EPR Spin System Parameters. Simulations and least-squares fitting (LSQ) were carried out with EasySpin toolbox (version 4.5.5) and Optimization Toolbox in MATLAB (Mathworks Inc., Natick, MA) using the routine chili for slow-motion cw-EPR spectra by solving the stochastic Liouville equation with rotational eigenfunctions as a basis.[42] The feasibility of changes in the rotational correlation time (τ_c) in distinguishing spin components was illustrated by simulating slow-motion spectra over isotropic τ_c values from 0.01 to 100 ns (Figure 2b and Table S1).

The best fits [P_{opt} (Table S2)] for spin system parameters (P) were determined by interfacing the EasySpin functions pepper (to determine g and A tensors for frozen samples) or chili (to determine rotational correlation times for ambient-temperature samples)[42] with MATLAB nonlinear least-squares (NLLS) routine lsqnonlin using the objective function obj(spectrum, P) defined below:

$$\text{obj(spectrum, } P) = [\text{spectrum}] - \text{rescale}[f(P, \text{exp}), \text{spectrum}]$$
$$f = \text{chili or pepper} \tag{3a}$$

For frozen samples, P(pepper) consists of rhombic g and A tensors as well as Gaussian and Lorentzian line widths, totaling eight parameters (Figure S8a). For ambient-temperature $N19C_{3IAP}$ and its corresponding $KaiBC_{EE}$ samples, P(chili) consists of a rotational correlation time (a = 1, 2, or 3) parameters (Figures S8b,c and S9). The use of lsqnonlin in place of Easyspin native NLLS function esfit[42] led to (i) reduced computational time, (ii) allowed user-defined lower and upper bounds for spin parameters as opposed to the [center ± vary] scheme, and (iii) enabled calculation of confidence intervals of spin parameters via the Jacobian matrix using the MATLAB function nlparci. We note that the Jacobian matrix-derived uncertainty measured only the depth or flatness of the local minimum in the objective function landscape with respect to P and thus could underestimate its uncertainty due to insufficient modeling or correlations in P. An alternative scheme was implemented via case resampling bootstrapping by magnetic field bootstrapping. In this scheme, the spectrum was first fitted as described above to obtain the best fit for P_{opt}. Then, 200 bootstrap spectra were generated via

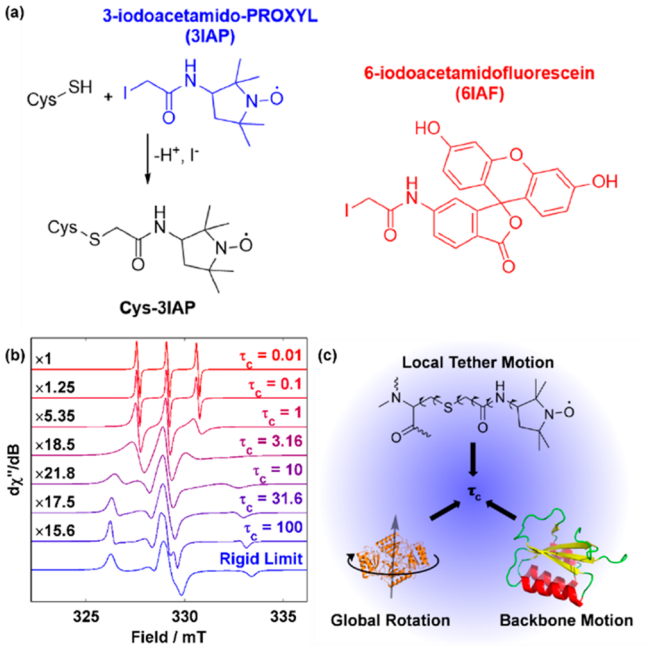

Figure 2. cw-EPR is a strategy for detecting and quantifying intermediates in the Kai clock. (a) Spin labeling reaction used to attach a nitroxide probe onto proteins of interest showing the spin-label 3-iodoacetamido-PROXYL (3IAP, blue) used in this work. The fluorophore 6-iodoacetamido-fluorescein (6IAF, red), also used in this work for fluorescence assays, is also shown for comparison. (b) Simulated nitroxide spectra as a function of mobility normalized by the maximum transition intensity. The scaling factor is shown to the left of each trace, whereas the isotropic rotational correlation time (τ_c in nanosecond) is shown at the right. Simulation details can be found in Table S1. (c) Three types of motions contribute to the experimentally observed rotational correlation time (τ_c), which reflects the mobility of the probe.

https://dx.doi.org/10.1021/acs.biochem.0c00279
Biochemistry 2020, 59, 2387−2400

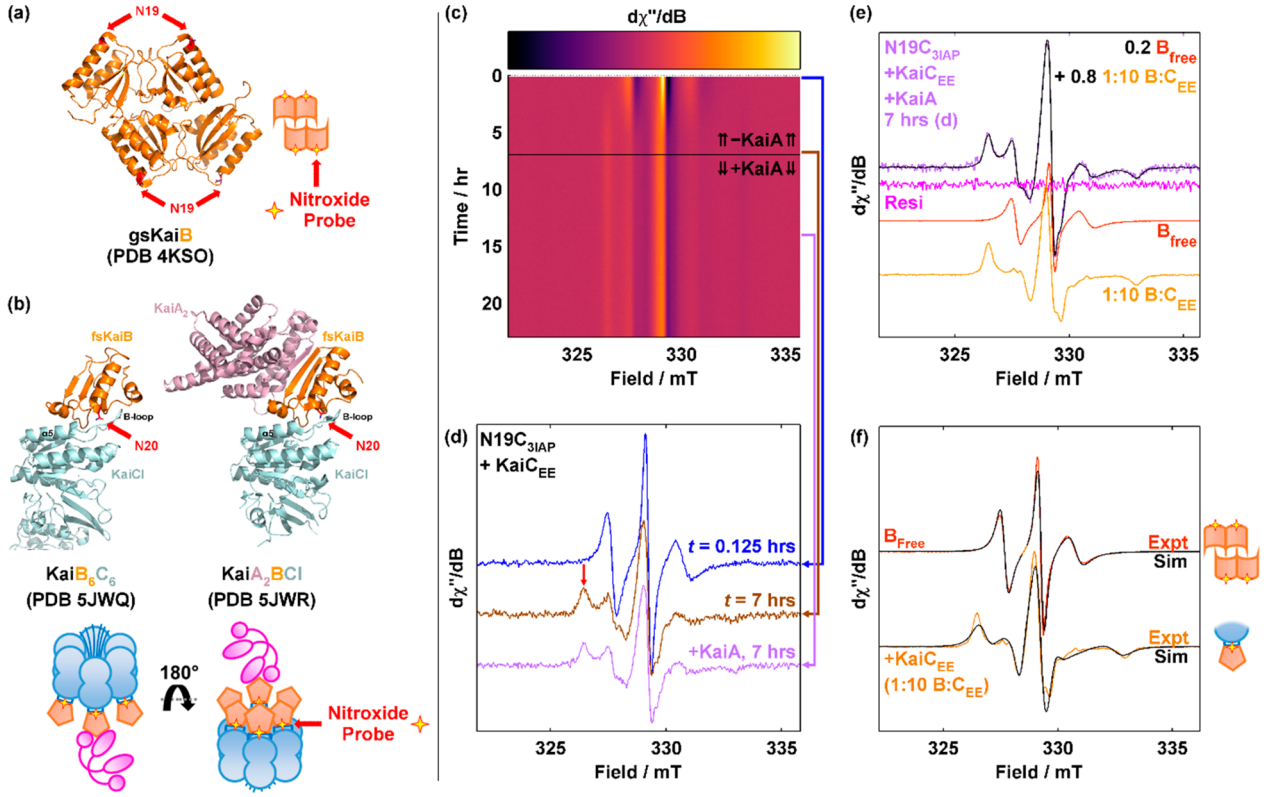

Figure 3. KaiB-N19C-3IAP ($N19C_{3IAP}$) reports KaiB−KaiC binding. (a) Crystal structure of tetrameric KaiB [Protein Data Bank (PDB) entry 4KSO] with N19 highlighted in red. (b) Crystal structures of $KaiB_6C_6$ (PDB entry 5JWQ, chains E and F) and $KaiA_2BCI$ (PDB entry 5JWR, chains A, B, E, and F) with N20 (PDB entries 5JWQ and 5JWR, *T. elongatus*) highlighted in red. Residue numbers of KaiB in PDB entries 5JWQ and 5JWR are offset from those of *S. elongatus* by +1. Color code: orange, KaiB; sky blue, KaiC; magenta, KaiA. Pictorial representations of the location of N19(N20) where 3IAP is installed are shown below the respective PDB codes. (c and d) cw-EPR spectra of $N19C_{3IAP}$ (5×, 17.5 μM) incubated with $KaiC_{EE}$ (17.5 μM) for 7 h and then spiked with KaiA (6 μM). Panel c shows a surface plot, whereas panel d shows a stacked plot at selected times. The red vertical arrow in panel d indicates B = 326 mT. (e) Reproduction of the experimental spectrum of $N19C_{3IAP}$ with $KaiC_{EE}$ and KaiA (7 h spectrum, lilac as in panel d)) with experimental spectra of free $N19C_{3IAP}$ (red) and $N19C_{3IAP}$ incubated with a 10-fold excess of $KaiC_{EE}$ (12 h, orange). (f) Overlay of spectral simulations (black) of free (red) and $KaiC_{EE}$-bound (orange) $N19C_{3IAP}$ using rhombic rotational correlation times. See Table S2 for simulation parameters.

randomly selecting magnetic field positions with replacement and performing NLLS using only the magnetic field positions specified and P_{opt} as a guess. The resultant fits P^* were then used to estimate the uncertainty in P. The $(1-2\alpha)$ confidence interval ($[L, U]$) of P will then have the form

$$L = 2P_{opt} - P^*_{(1-\alpha)};\ U = 2P_{opt} - P^*_{(\alpha)} \tag{3b}$$

where $P^*_{(0.01\gamma)}$ refers to the γth quantile of P^*.

To facilitate ambient-temperature simulations, the g and A tensors were first determined in the near-rigid limit at −40 °C in a 20% (w/w) sucrose (20 Bx) solution using the EasySpin function pepper (Figure S8a) with their uncertainties estimated as described above. The 30 °C spectra were then fitted with fixed g and A tensors with reduced line widths while floating their rotational correlation time(s). For both free and KaiC-bound KaiB, their spectra were simulated with isotropic, axial, and rhombic rotational correlation times in that order (Figure 3f and Figure S8b,c). For selectivity testing of KaiB with respect to direct KaiB−KaiA binding (Figure S9), spectral subtraction was employed by subtracting the spectrum of free KaiB from the reaction spectrum of a 10-fold excess of KaiA and the resultant spectrum was simulated as described above (also see the Supplementary Text). The necessity of rotational anisotropy in simulations was tested via an F-test and AIC computed using the formulas below:

$$F_{aniso/iso} = \frac{NRMSD_{iso}^{\ 2} - NRMSD_{aniso}^{\ 2}}{NRMSD_{aniso}^{\ 2}} \times \frac{df_{aniso}}{df_{iso} - df_{aniso}} \tag{4a}$$

$$df_{iso} = 1023;\ df_{aniso} = 1023 - k,\ k = \begin{cases} 1, \text{ axial} \\ 2, \text{ rhombic} \end{cases} \tag{4b}$$

where NRMSD refers to the normalized root-mean-square deviation and is the square root of the residual sum of squares (RSS), normalized by the sum of squares of the background-corrected spectra. For AIC model selection, the quantity of adjustable parameters is equal to $k + 2$ due to the contribution from isotropic rotation and noise. The AIC is calculated by

$$AIC = 2(k + 2) - 2\ln(\hat{L}) \tag{4c}$$

where the log-likelihood $\ln(\hat{L})$ is computed by

$$\ln(\hat{L}) = -\frac{n}{2}\ln(2\pi) - \frac{n}{2}\ln\frac{RSS}{2} - \frac{n}{2},\ n = 1024 \tag{4d}$$

Due to the possibility for the slight temperature- and local environment-dependent nature of g and A, the spin parameters were further floated within small constraints to better fit the data and compared with the results derived from floating only the rotational correlation time (Figure S8b,civ). It was

https://dx.doi.org/10.1021/acs.biochem.0c00279
Biochemistry 2020, 59, 2387−2400

observed that significantly better fits were obtained by floating g and A, but the values obtained deviated from those of typical nitroxide spin-labels in aqueous solutions determined from multifrequency studies[40] and thus were not further considered.

Quantitative Weight Fitting for N19C$_{3IAP}$. The microwave frequency drift-corrected real-time cw-EPR data $Y_{1024\times n}$ were simulated by varying the weights (w_{ij}) of the r components as represented by the matrix multiplication in eq 5, where $B_{1024\times r}$ corresponds to the spectra of the r components and w_{ij} corresponds to the weight of the ith species in the jth spectrum ($i = 1-r$; $j = 1-n$):

$$Y_{1024\times n} = B_{1024\times r} w_{r\times n} + \varepsilon_{1024\times n} \tag{5}$$

where ε represents the residual of the fit. The background-corrected spectra of 35 μM spin-labeled KaiB in reaction buffer and 17.5 μM KaiB (5×) in equilibrium with a 10-fold excess of KaiC$_{EE}$ were taken as $B_{free,unscaled}$ and B_{bound}, respectively. In general, two spectra may differ in total intensity due to differences in concentration/volume due to experimental design and/or pipetting error, sample alignment, Q factor, or other unexplained factors. The $B_{free,unscaled}$ and B_{bound} obtained thus cannot be directly used for quantification and must be scaled or normalized. Double integration-based normalization was avoided due to known numerical instability and susceptibility to noise (see Figure S10a).[43] Instead, the spectra were normalized by using the real-time kinetic data of KaiB in the presence of a 10-fold excess of KaiC$_{EE}$. The real-time data can be written as

$$Y = \begin{pmatrix} B_{free,scaled} & B_{bound} \end{pmatrix} \begin{pmatrix} 1 - w_t \\ w_t \end{pmatrix} = \begin{pmatrix} \theta B_{free,unscaled} & B_{bound} \end{pmatrix}$$
$$\begin{pmatrix} 1 - w_t \\ w_t \end{pmatrix} = \begin{pmatrix} B_{free,unscaled} & B_{bound} \end{pmatrix} \begin{bmatrix} \theta(1 - w_t) \\ w_t \end{bmatrix} \tag{6}$$

where θ is the scaling factor to scale B_{free}. B_{bound} is set to be the mean of all spectra in the window t = 12−24 h where there is complete binding. Under these conditions, w_t tends toward unity as binding goes to completion as the spectrum is dominated by B_{bound}. The equation implies that w_t and $\theta(1 - w_t)$ can be solved via linear regression (Figure S10b). As $B_{free,unscaled}$ is not scaled, the weight coefficients do not add up to unity. θ can then be solved via linear regression by plotting $\theta(1 - w_t)$ against $1 - w_t$ (Figure S10c). B_{free} is then scaled by θ (Figure S10d).

In addition to B_{free} and B_{bound}, background spectrum B_{bg} and constant/linear correction terms B_{b0} and B_{b1} were included. Thus, for a cw-EPR spectrum Y_j that contains two components KaiB$_{free}$ and KaiB$_{bound}$, the equation is overdetermined (1024 equations, 5 unknowns). The corresponding normal equation is

$$w_j = (B^T B)^{-1} B^T Y_j,\ B = \begin{pmatrix} B_{free} & B_{bound} & B_{bg} & B_{b0} & B_{b1} \end{pmatrix} \tag{7a}$$

The shape of each component can be found in Figure S11c. The weights are reported as ratios to total nitroxide content (a_{ij}).

$$a_{ij} = \frac{w_{ij}}{\sum_{k=1}^{r} w_{kj}};\ \sum_{i}^{r} a_{ij} = 1 \tag{7b}$$

We noted that simulations of spectra from technical replicates using experimental spectra of pure KaiB and KaiBC$_{EE}$ as basis spectra (B) occasionally led to slight magnetic field offsets ("B-shift") that could not be accounted for even after correcting for changes in microwave frequency. We reason that these differences were due to (1) minor variations in magnetic shielding between experiments, (2) removing and reinserting the variable-temperature Dewar, and/or (3) ambient-temperature drift leading to minor magnetic field output. To determine the variation in "B-shift" over time, 20 μM 4-hydroxy-TEMPO (TEMPOL) was used as a spin standard (Figure S6a). It was found that the spectrum drifted horizontally over a 3 day period even after accounting for microwave frequency drift (Figure S4a,b). This drift was correlated to ambient-temperature changes and had a period of ∼24 h but with a lag of 5 h (Figure S6b), hinting that the origin of this time-dependent "B-shift" was potentially due to periodic drift in (1) magnet temperature, (2) expansion or contraction near the magnet, and/or (3) circuit load on the electrical outlets supplying the magnet, all of which can result in variations in magnetic field output.

Because minor shifts in the magnetic field abscissa directly impact spin quantification (Figure S6c), the experimental spectra were shifted horizontally (B') to account for this difference. The discrete form of this shift can be written as a matrix operator P below:

$$B_i' = P^{n_i} B_i,\ P = \begin{pmatrix} 0 & \cdots & 0 & 0 \\ 1 & \cdots & 0 & 0 \\ \vdots & \ddots & 0 & 0 \\ 0 & \cdots & 1 & 0 \end{pmatrix} \tag{8a}$$

As the optimal shift (in millitesla) is unlikely to be an integer multiple of the magnetic field unit, the magnitude of the shift n_i may take any real value s and is achieved via interpolation. Hence, quantitative cw-EPR at any time t becomes a nonlinear problem of 1024 equations and r + 1 unknowns:

$$\min_{w_t, s_t} [\text{shift}(Y, s_t) - B_{1024\times r} w_{t,r\times 1}] \tag{8b}$$

Hence, simultaneously solving for w_t and s_t yields the weights of each component and the "B-shift" provided that the spectra of the components were known and "B-shift" corrected. However, eq 5 did not explicitly take "B-shift" into account. Accordingly, eq 5 is modified to the following:

$$Y_t = \text{shift}\left[\sum_{i=1}^{r} \text{shift}(B_i w_{it}, s_i), s_t\right] + \varepsilon \tag{9}$$

where Y_t and s_t are the spectrum and "B-shift" magnitude at time t, respectively, w_{it} is the weight of the ith component at time t, and s_i is the component-dependent shift. The term s_i accounts for the intersample "B-shift" contribution due to changes in sample placement and thus effective magnetic field experienced at the sample, whereas s_t accounts for intrasample "B-shift" due to fluctuations in magnetic field output that was found to correlate with ambient temperature (Figure S6b). Nonlinear least squares is used to solve for w_{it}, s_i, and s_t simultaneously by considering data at multiple time points (t_n) using the components $B_{free,unscaled}$, B_{bound}, and B_{bg}. This results in 1024 × n equations and 3n (w_{it}) + (3 − 1)(s_i) + n(s_t) unknowns with initial guesses for w_{ij} obtained via linear regression and s_i and s_t set to zero. Only r − 1 components require a non-zero s_i as s_i and s_t co-vary and $s_{i=1}$ is hence defined to be zero. The fitted w_{it} is then used to compute θ (eq

https://dx.doi.org/10.1021/acs.biochem.0c00279
Biochemistry 2020, 59, 2387−2400

6) for scaling, whereas s_i is used to shift the B components for further quantitative analysis (eq 8b).

Uncertainty Analysis in Quantitative Real-Time cw-EPR Kai Reactions. There are three contributions to the observed variance in the data: (1) spin model/spectral line shape uncertainty, (2) noise-induced uncertainty, and (3) other random errors, including pipet errors and protein batch-to-batch variability.

(1) Spin Model/Spectral Line Shape Uncertainty (σ_{model}). Although experimental spectra were used for fitting of all real-time spectra, giving rise to well-defined line shapes, the necessity of scaling B_{free} relative to B_{bound} introduces error in the form of uncertainty in scaling factor θ. As θ is determined via linear regression (eq 6), the confidence interval in θ can be readily obtained by standard linear regression formulas and implemented by MATLAB function regress.

(2) Noise-Induced Uncertainty ($\sigma_{S/N}$). Real data are noisy and thus give rise to uncertainty in quantification. The weights of B_{free} and B_{bound} are simultaneously determined with "B-shift" via nonlinear regression (see eq 8b). Uncertainty can thus be estimated via the Jacobian matrix and MATLAB function nlparci.

(3) Other Random Errors (σ_r). Other random errors include protein batch-to-batch variations, pipetting error, and other unknown sources of error. This error can be observed when comparing results obtained between technical replicates.

For phosphomimetic reactions, the overall uncertainty is then computed as

$$\sigma_{tot}^2 = \sigma_{model}^2 + (\sigma_{S/N}^2 + \sigma_r^2) \tag{10a}$$

The modeling or line shape uncertainty error is intrinsic to the data processing. On the other hand, performing multiple technical replicates simultaneously measures σ_r and $\sigma_{S/N}$.

For oscillator reactions, direct averaging of multiple replicates can lead to cancellations in oscillations due to minor variations in period and/or phasing. Thus, calculation of the inter-replicate standard error of the mean (SEM) was not performed. Instead, the error reported does not contain inter-replicate uncertainty:

$$\sigma_{tot}^2 = \sigma_{model}^2 + \sigma_{S/N}^2 \tag{10b}$$

Uncertainty estimates from the Jacobian matrix obtained from nonlinear least-squares correspond to weights (w) to be converted to fractions (a). This propagation is done via

$$(\delta a_i)^2 = \sum_{j=1}^{n}\left(\frac{\partial a_i}{\partial w_j}\cdot\delta w_j\right)^2 = \frac{w_i^2}{(\sum w)^4}\sum_{j=1}^{n}\delta w_j^2 + \delta w_i^2\left[\frac{1}{(\sum w)^2} - \frac{2w_i}{(\sum w)^3}\right] \tag{11}$$

where w_i in eq 11 corresponds to the weight of component i in the spectrum and a_i corresponds to the ratio of component i to the overall concentration. Notice that the first term is common for all values of i and j whereas the second term is a correction term arising from the $i = j$ case in the summation. The final 95% confidence interval (CI) is calculated by

$$a = \bar{a} \pm \sqrt{(t_{0.975,df}\sigma_{model})^2 + (z_{0.975}\sigma_{S/N})^2} \tag{12}$$

where $\bar{a}$ is the best estimate for a and $t_{0.975,df}$ and z are t and z values, respectively, for the 95% confidence interval, where df refers to the degrees of freedom in the evaluation of θ.

In experiments in which the binding velocity was desired to be computed (see Figures S11 and S12), a Savitzky–Golay filter was applied via Easyspin function savgol to simultaneously smooth and differentiate the binding kinetic curve using seven-point window and quadratic polynomials.

Circadian Oscillation Rhythm Period and Waveform Analysis. The extracted KaiB binding kinetics were further analyzed by curve fitting to mFourfit[44] (MFF) by modeling the kinetic trace $f(t)$ as a sum of cosines as shown below using lsqnonlin as the interface:

$$f(t) = C + \sum_{j=1}^{q} A_j \cos\left[\frac{2\pi j(t-\varphi_j)}{T}\right] + \varepsilon;\ q = 1{-}4 \tag{13a}$$

where the constant C, amplitude A_j, phase angle φ_j, and period T are adjustable parameters and the residual term ε is minimized. The quantity of cosines used can be adjusted by changing q. The number of adjustable parameters is thus equal to $3 + 2q$. To prevent overfitting, the corresponding AIC was computed at each q by

$$\mathrm{AIC}(q) = 2(3 + 2q) - 2\ln(\hat{L}) \tag{13b}$$

Confidence intervals in amplitude and period were determined with nlparci. To ascertain the period of oscillation, the maximum entropy spectral analysis (MESA)[45] and Lomb–Scargle periodogram[46] were computed and compared with the period obtained via MFF (Figure S15b,c).

RESULTS

cw-EPR Strategies for Quantifying Complex Mixtures.

As cw-EPR spectra of mixtures are additive, quantitative kinetics can be extracted from real-time cw-EPR experiments with spin-labeled proteins if the spectra of underlying components are known. Thus, successful cw-EPR quantification is contingent upon design and/or discovery of spectroscopic handles that respond to relevant interactions. Because none of the Kai proteins contain paramagnetic centers necessary for direct cw-EPR characterization, a spin-label in the form of nitroxide can be introduced via bioconjugation to provide this handle. This is most conveniently done via site-directed mutagenesis to cysteine followed by labeling with a cysteine-reactive reagent that bears the nitroxide moiety (Figure 2a). In this regard, KaiB is an ideal candidate for spin labeling due to its lack of native cysteine residues as compared to KaiA (six cysteines per monomer) or KaiC (three cysteines per monomer).

There are multiple strategies for designing a labeling site such that the nitroxide spectroscopic handle will respond to binding once installed on the protein of interest by exploiting various spin-based phenomena. One such strategy is to install spin-labels that are close to one another in a multimeric protein, resulting in spin exchange[47] and/or dipolar broadening[48] that broadens the spectra and thus differentiates monomeric versus multimeric species. Another strategy that is exploited in this work is the mobility dependence of the width of the nitroxide spectrum. Unlike the free nitroxide molecule in solution that tumbles freely, a protein-bound nitroxide moiety exhibits a reduced level of global tumbling. Motions originating from the connecting tether and protein backbone dominate. As

https://dx.doi.org/10.1021/acs.biochem.0c00279
Biochemistry 2020, 59, 2387–2400

the motion slows from rapid tumbling toward the rigid limit, the ^{14}N hyperfine anisotropy is no longer averaged out by the motion and the cw-EPR spectrum broadens (Figure 2b). This mobility as quantified by the rotational correlation time (τ_c) of a spin-labeled residue is a combination of local and global motions (Figure 2c), changes in which are directly reflected in cw-EPR spectra (Figure 2b). Thus, a successful spin labeling site should lead to either (a) a nitroxide tether that becomes motionally restricted or (b) a change in secondary structure on protein−protein binding. In theory, the global protein tumbling motion (Figure 2c) should contribute to experimentally observed mobility as predicted by the Stokes−Einstein relation (SE, τ_c^{SE}):

$$\tau_c^{SE} = \frac{\eta V}{k_B T} = \frac{\eta M_p \bar{\nu}_p}{k_B T} \quad (14)$$

where η is the dynamic viscosity of the buffer (assumed to be equal to that of water at 30 °C), V is the estimated volume of the crystal structures, $\bar{\nu}_p$ (= 0.73 cm^3 g^{-1}) is the partial specific volume, M_p is the molecular weight of the protein, k_B is the Boltzmann constant, and T is the temperature in kelvin. In practice, τ_c^{SE} often underestimates global rotation by a factor of 2 due to the negligible level of hydration.[49] This puts a lower limit on the molecular mass of the protein in question as nitroxide spectra stemming from spin-labeled proteins smaller than this limit will be influenced by both local mobility and global rotation. The parallel contributions from both local and global motions complicate interpretations as spectral changes can no longer be attributed to only local binding events.

Site Design and Other Practical Considerations in SDSL−cw-EPR for Probing KaiB−KaiC Binding. Like fluorescence anisotropy (FA),[36] the success of EPR spin labeling-based assays is dependent on the labeling site. In the former, site design is guided by two potentially conflicting principles that both local rotational effects ("propeller effects") and binding affinity interference should be minimized.[50] In the latter, it is precisely the changes in local rotational motion that enable a meaningful binding assay as reflected by nitroxide line shape changes while also taking advantage of the smaller footprint of a nitroxide moiety compared to common fluorophores (Figure 2a). To that end, we chose KaiB-N19 (Figure 3a) as the mutation site for studying KaiB−KaiC binding without interference from KaiA. N19 is located at the N-terminal cap of KaiB-α1 and is close to the KaiB-CI binding interface in published crystal structures (Figure 3a).[21] However, it is pointed away from the KaiB−KaiA binding interface in the ternary KaiABC complex (Figure 3b).[21] Hence, we hypothesized that the N19C mutant of KaiB when spin-labeled will report a decrease in flexibility on KaiB−KaiC binding but that further binding to KaiA will not report the ternary KaiABC complex as a spectroscopically distinct species.

To generate the spin-labeled KaiB-N19C-3IAP construct ($N19C_{3IAP}$ hereafter), a 5-fold excess of TCEP was first added to unlabeled KaiB to reduce preformed disulfide bonds that prevent cysteine-iodoacetamide bioconjugation. Then, a 10-fold excess of 3IAP was added. The labeling efficiency can be checked by intact mass spectrometry (Figure S1). As the EPR signal intensity varies with the quantity of spins in a sample, the labeling reaction should be repeated on samples with low labeling efficiencies to drive the labeling reaction toward completion to provide an optimal signal-to-noise (S/N) ratio. The more commonly used spin-labels *S*-(1-oxyl-2,2,5,5-tetramethyl-2,5-dihydro-1*H*-pyrrol-3-yl)methylmethanesulfonothioate (R1) and 4-maleimido-TEMPO (4MT) were avoided because they release free PROXYL via disulfide exchange when encountering free thiols[51−53] and undergo maleimide hydrolysis to the more flexible succinamic acid ester (SAT),[54,55] respectively, rendering them unsuitable for functional assays that span multiple days.

Despite the enhanced reactivity between $N19C_{3IAP}$ and $KaiC_{EE}$ as compared to WT-KaiB as revealed by native-PAGE (Figure S2) on mutagenesis and spin labeling, wild-type KaiB could be completely replaced by $N19C_{3IAP}$ without significantly altering the period of the Kai oscillator based on our previously developed FA assay using 6IAF-labeled KaiB-K25C as a fluorescence reporter [$K25C_{6IAF}$ (Figure S3)].[36] Our spin-labeled KaiB mutants are thus robust functional surrogates for wild-type KaiB and therefore suitable as reporters of the Kai clock.

The Spin-Labeled Construct Provides a Selective Response to KaiB−KaiC Binding. To test our hypothesis that $N19C_{3IAP}$ provides a spectroscopic handle for quantifying KaiB−KaiC binding without interference due to ternary KaiABC complex formation, $N19C_{3IAP}$ was first reacted with a stoichiometric amount of $KaiC_{EE}$ and then the mixture was spiked with KaiA after 7 h (Figure 3c,d). $KaiC_{EE}$, a $KaiC_{pSpT}$ phosphomimetic, was chosen as the KaiC surrogate as S431 phosphorylation was shown to be necessary for KaiBC complex formation, and $KaiC_{EE}$ outperformed $KaiC_{EA}$ in binding to KaiB.[23] As spectra from the same sample were collected at 7.5 min intervals over 24 h, 192 spectra were recorded and displayed as a surface plot (Figure 3c). Comparison between cw-EPR spectra recorded immediately after mixing $N19C_{3IAP}$ and $KaiC_{EE}$ versus that of a sample that had been incubated for 7 h (Figure 3d and Figure S7) revealed the formation of a slowly tumbling species in the latter as indicated by the appearance of a peak at 326 mT that is identified as originating from KaiB−KaiC interactions. The intensity of this peak reached a maximum in approximately 6 h (Figure 3c), in agreement with native-PAGE (Figure S2). When the sample was spiked with KaiA, the intensity of the slowly tumbling species decreased marginally but no new spectroscopically distinct species were visually discernible (Figure S7a). Furthermore, the real-time KaiB−$KaiC_{EE}$−KaiA reaction spectra could be satisfactorily reproduced as a linear combination of the spectrum of pure $N19C_{3IAP}$ and that of $N19C_{3IAP}$ in a 10-fold excess of $KaiC_{EE}$ (Figure 3e and Figure S7b). This implies that cw-EPR of $N19C_{3IAP}$ does not distinguish between various $KaiA_{2j}B_iC_6$ complexes (i = 1−6, and j = 0−i),[27,28,56] and thus, the spectra derived from $N19C_{3IAP}$ and KaiC can be used as a readout reflecting the fraction of KaiC-bound KaiB independent of KaiA forming a complex with KaiBC.

To investigate the origin of the observed equivalence of cw-EPR spectra of $N19C_{3IAP}$ in KaiABC complexes of various stoichiometries, spectral simulations were applied to analyze the rotational motion of the KaiB-bound spin-labels. The best fits for free and $KaiC_{EE}$-bound $N19C_{3IAP}$ are shown in Figure 3f. The g and A tensors determined at the near-rigid limit at −40 °C using 20% (w/w) sucrose (Figure S8a and Table S2) are highly comparable to those obtained via W-band cw-EPR (94 GHz) of 3IAP[57] as well as multifrequency studies of the related spin-label R1.[40] Although the Brownian-motion model oversimplifies the spin-labeled systems in question as global rotation, backbone, and local tether motions are all known to

https://dx.doi.org/10.1021/acs.biochem.0c00279
Biochemistry 2020, 59, 2387−2400

contribute to rotational diffusion (Figure 2c), experimental spectra of both free and $KaiC_{EE}$-bound $N19C_{3IAP}$ acquired at 30 °C could be satisfactorily simulated via such treatment and hence justify its application. The effective isotropic correlation times ($\tau_c^{iso,eff}$) of both forms of $N19C_{3IAP}$ are shorter than their Stokes−Einstein (SE) estimates [τ_c^{SE} (Figure S8b,c and Tables S2 and S3)]. Similar observations have been demonstrated with 3IAP-labeled IDPs[57] and R1-labeled lysozyme.[40] As typical rotational correlation times estimated by SE often underestimate τ_c^{iso} by a factor of 2 for globular proteins,[49] our simulations imply that the combined motions of the nitroxide tethers and protein backbone in both free and KaiC-bound KaiB exhibit high flexibility as the tethered nitroxide probe moves faster than global rotational motion. The experimentally observed τ_c^{eff} is thus attributed to the combined motions of the nitroxide tether and protein backbone and explains the independence of the spectral signature to $N19C_{3IAP}$−KaiC binding stoichiometry.

For the sake of completeness, we also reacted $N19C_{3IAP}$ with KaiA in the absence of KaiC to determine its spectral sensitivity to direct KaiA−KaiB interactions (Figure S9). It has previously been reported that KaiA could bind to WT-KaiB in trace quantities in the form of $KaiA_2B_1$ based on native mass spectrometry.[28] Separately, mutations that destabilize tetrameric gs-KaiB via either the G88A mutation[24] or C-terminal deletions[20] have been shown to enhance direct KaiA−KaiB interactions. On the basis of these observations, it is deduced that KaiB likely adopts the fs-KaiB conformation in the $KaiA_2B_1$ complex. To determine if $N19C_{3IAP}$ responds to direct KaiA−KaiB interactions, cw-EPR spectra of 17.5 μM $N19C_{3IAP}$, corresponding to 5× in vitro oscillator, in the presence of varying concentrations of KaiA were compared. The cw-EPR spectrum in the presence of 6 μM KaiA (5×) could not be discerned from that of $N19C_{3IAP}$ alone (Figure S9a). There are three possibilities to this observation. (a) KaiB and KaiA do not interact at all. (b) They interact, but X-band cw-EPR of $N19C_{3IAP}$ treats the KaiA-bound KaiB population as spectroscopically equivalent to free KaiB. (c) They interact to give a spectroscopically distinct species, but the limited S/N ratio renders detection impossible. The last scenario may be attributed to (i) weak interactions at the physiologically relevant KaiA:KaiB ratio (1:3) and/or (ii) the high degree of cw-EPR spectral similarity between free and KaiA-bound $N19C_{3IAP}$ due to insignificant changes in local mobility. In an attempt to distinguish the three scenarios and drive KaiA−KaiB interactions, we increased the KaiA:KaiB ratio to 10:1 and observed subtle changes in the h_{-1} transition region as well as slight broadening in the central transition (Figure S9b), ruling out possibilities (a) and (b). Subtraction and simulation studies indicate that this motional component constitutes at least 7% of the total signal under excess KaiA loading (Figure S9c, Table S4, and the Supplementary Text). Because this ratio is unphysiological as ratios of 1:3[29] to 1:30[22] have been reported in vivo, little insight into the biological relevance of direct KaiA−KaiB interactions can be gained. Nevertheless, the selectivity of the spectroscopic response of $N19C_{3IAP}$ to KaiB−KaiC interactions is established.

Quantitative Interpretation of KaiB−KaiC Binding. Because $N19C_{3IAP}$ is the only EPR-active species in the experiments described above, the fraction of KaiB in KaiC-bound KaiB relative to total KaiB is equal to its contribution (weight) normalized by the total weight of the spectrum. It was found above that the $N19C_{3IAP}$ reaction spectra could be explained by two components, free and KaiC-bound KaiB (Figure 3e). The former was readily obtained by acquiring the spectrum of $N19C_{3IAP}$ alone, whereas the latter was obtained by adding it to a 10-fold excess of $KaiC_{EE}$ (Figure S7b). Quantitative kinetics with $N19C_{3IAP}$ could thus be extracted using these two spectra as basis spectra.

We first applied this strategy to analyze the KaiB−$KaiC_{EE}$ binding data to obtain a binding progression curve. The extracted kinetics exhibited sigmoidal kinetics (Figure 4a and

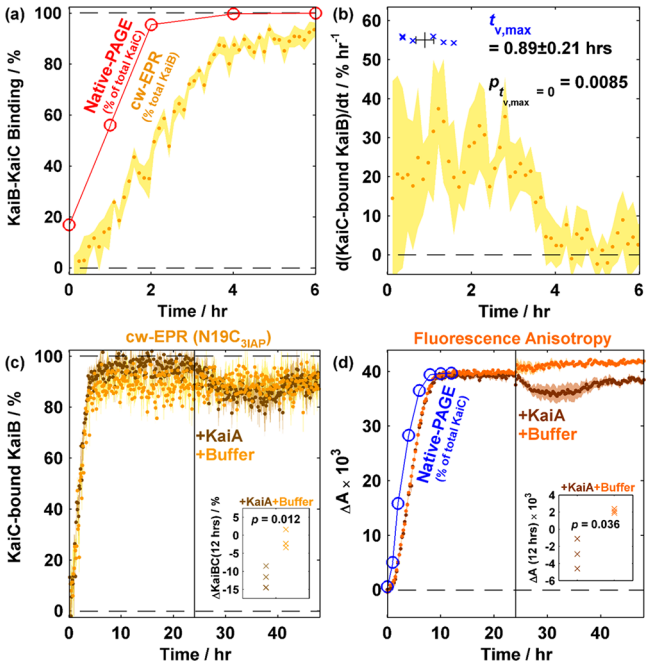

Figure 4. cw-EPR is an orthogonal method for quantitatively assaying KaiB−KaiC binding as illustrated by KaiB−$KaiC_{EE}$ binding followed by KaiA spiking at 24 h. (a) Overlay of $N19C_{3IAP}$−$KaiC_{EE}$ binding kinetics obtained via native-PAGE (red empty circles) and cw-EPR (yellow filled circles) from 0 to 6 h. (b) Rate of formation of KaiC-bound KaiB (yellow circles) and time at maximum binding velocity ($t_{v,max}$, blue crosses). For panels a and b, the shaded area (cw-EPR) and error bars ($t_{v,max}$) indicate SEM (n = 6). (c) Overlay of $N19C_{3IAP}$−$KaiC_{EE}$ cw-EPR binding kinetics followed by spiking with KaiA (brown) or buffer (yellow) at 24 h. Shaded areas show the SEM (n = 3). (d) Overlay of WT-KaiB−$KaiC_{EE}$ fluorescence anisotropy-based binding kinetics using 50 nM KaiB-K25C-6IAF ($K25C_{6IAF}$) as a fluorescence probe with KaiA (brown) or buffer (orange) spiking at 24 h. Shaded areas show the SEM (n = 3). Insets in panels c and d show two-tailed t-tests comparing the effects of KaiA vs buffer spiking after 12 h of spiking. cw-EPR data were binned in 2 h bins prior to performing the t-test.

Figures S11 and S12). Qualitatively, the sigmoidal kinetics observed in our experiments rules out the possibility of single-step KaiB−KaiC binding and is consistent with previous studies that indicate binding cooperativity among KaiB subunits[27] as well as gating via KaiB fold switching and/or CI ATPase activity.[24] To quantify binding latency, we determined the time taken to reach the maximum rate of binding ($t_{v,max}$) to be 0.9 ± 0.2 h [SEM; n = 6 (Figure 4b and Figures S11 and S12)]. Compared to native-PAGE (Figure S2), the nondestructive nature of ambient-temperature cw-EPR allows kinetics to be determined using a single sample. This contrasts with native-PAGE in which the sample is adulterated by the loading buffer and consumed during

https://dx.doi.org/10.1021/acs.biochem.0c00279
Biochemistry 2020, 59, 2387−2400

electrophoresis, rendering the need to prepare multiple samples flash frozen at predetermined times. The improved time resolution of cw-EPR over native-PAGE allows identification of sigmoidal kinetics in $N19C_{3IAP}$–$KaiC_{EE}$ binding that is not observed in native-PAGE.

Curiously, an apparent offset of approximately 1 h was observed between kinetics derived from cw-EPR versus native-PAGE (Figure 4a). As KaiC (58 kDa) is larger than KaiB (11 kDa), the native-PAGE band intensity is likely dominated by KaiC in KaiBC complexes. Furthermore, native-PAGE electrophoretic mobility is a function of protein conformation. We interpret the discrepancy in native-PAGE and either cw-EPR or FA (Figure 4d and Figure S13, vide infra) as originating from the former being sensitive to KaiC conformational changes in KaiB binding. This discrepancy is consistent with the multistep nature of KaiB–KaiC binding based on native mass spectrometric identification of substoichiometric KaiBC complexes.[27] However, the possibility of in-gel KaiB–KaiC binding during electrophoresis cannot be ruled out.

We further analyzed the KaiB–$KaiC_{EE}$ binding data when the steady-state mixtures were subjected to KaiA spiking (Figure 4c and Figures S11 and S12). On the basis of previous studies, the addition of KaiA to an equilibrated mixture of KaiB and $KaiC_{EE}$ would lead to a ternary mixture of KaiB-containing species: KaiB, $KaiBC_{EE}$, and $KaiABC_{EE}$.[20] As demonstrated above, cw-EPR of $N19C_{3IAP}$ is insensitive to KaiABC complexes due to the lack of formation of spectroscopically distinct species at physiologically relevant concentrations. Thus, the slight increase in the mobile component's intensity after KaiA was added to the preequilibrated mixture of $N19C_{3IAP}$ and $KaiC_{EE}$ provides unequivocal evidence that KaiA can antagonize $KaiBC_{EE}$ interactions slowly (Figures 3d and 4c and Figures S11 and S12). On the contrary, interpretation of the $K25C_{6IAF}$ FA data (Figure 4d and Figure S13) is complicated by the presence of at least three KaiB-containing species even under the assumption that KaiBC complexes of all stoichiometries ($KaiB_iC_6$, where i = 1–6) have identical fluorescence anisotropies. Because there is little theoretical basis to assume that $K25C_{6IAF}$ in the ternary $KaiABC_{EE}$ complex possesses an FA identical to that of the binary $KaiBC_{EE}$ complex, the use of FA to quantify KaiB–$KaiC_{EE}$ binding in the presence of KaiA is akin to solving an underdetermined system of equations. Nevertheless, if these assumptions hold, we anticipate that formation of the ternary complex would marginally increase the observed anisotropy whereas KaiB–KaiC interaction antagonization should reduce the anisotropy. The observed decrease in anisotropy could thus be interpreted qualitatively as $KaiBC_{EE}$ complex antagonization, a fortuitous conclusion that agrees with cw-EPR-derived kinetics (Figure 4c and Figures S11 and S12). This KaiA spiking experiment highlights the potential ambiguity in extracting kinetics from single-wavelength FA data. On the other hand, cw-EPR benefits from the use of the magnetic field as a second abscissa, offering the possibility of statistically testing the quantity of components via rank analysis[58] and quantifying more than two components if warranted. Thus, cw-EPR of spin-labeled KaiB offers an orthogonal and quantitative method for probing KaiB–KaiC binding while eliminating interference due to ambiguity in variable Kai protein stoichiometries.

Application to Oscillator Reactions. Equipped with the knowledge that $N19C_{3IAP}$ probes KaiB–KaiC binding, we measured the time dependence of KaiB binding in the in vitro oscillator using real-time cw-EPR (Figure 5 and Figures S14–S16) using $N19C_{3IAP}$ as a spin-labeled surrogate for WT-KaiB.

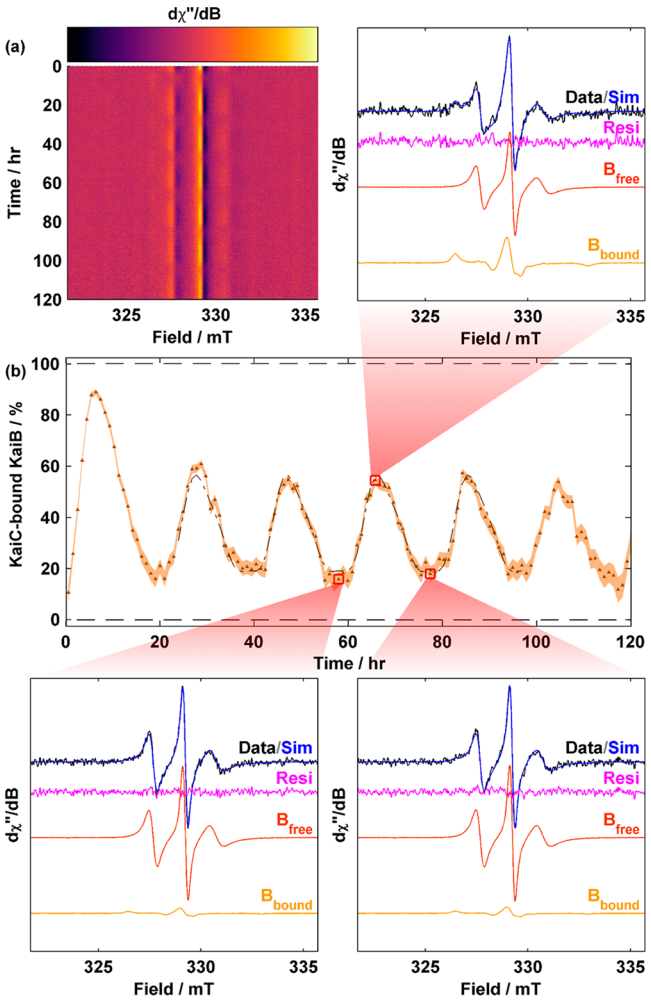

Figure 5. Observation of KaiB–KaiC binding and dissociation throughout the Kai oscillations via cw-EPR. (a) Surface plot of cw-EPR spectra of $N19C_{3IAP}$ 1× oscillator (3.5 μM $N19C_{3IAP}$, 3.5 μM KaiC, and 1.2 μM KaiA). (b) cw-EPR-based kinetics of KaiC-bound KaiB as a function of time. Data were binned in 1 h bins. The shaded area indicates the 95% CI. A fit to the sum of cosines is overlaid as a dashed–dotted line (see Table S5). Selected spectra at three time points (red squares) with their respective fit are displayed.

The cw-EPR spectra of $N19C_{3IAP}$ in the reconstituted oscillator demonstrated periodic time dependence as seen in height oscillations of the central (h_0) transition at B_0 = 329.1 mT as well as broader features corresponding to h_{-1} and h_{+1} transitions that are out of phase with the h_0 transition (Figure 5a and Figure S14a). The periodic spectral variations indicate periodic KaiB binding–unbinding events. Although individual spectra at a 1× concentration were very noisy, reasonable fits using experimental spectra of pure KaiB and $KaiBC_{EE}$ were still possible after binning (Figure 5b and Figure S14b) and enabled quantitative determination of binding progression with high reproducibility (Figure S15). Using a sum of cosines via mFourfit[44] (Figure S16), we determined the phenomenological amplitude of oscillation to be 41.7 ± 3.4% [SEM; n = 4 (Figure 5b, Figure S15, and Table S5], slightly smaller than 50% as determined by FCS by Goda et al.[34] We reasoned that the minor discrepancy is due to a smaller translational diffusion

https://dx.doi.org/10.1021/acs.biochem.0c00279
Biochemistry 2020, 59, 2387–2400

coefficient of the ternary KaiABC complex compared to KaiBC that leads to amplitude overestimation in a two-component model. However, the difference in reactivity between WT-KaiB and $N19C_{3IAP}$ revealed by native-PAGE (Figure S2) may also contribute to the difference in amplitudes. The overall shape of the binding curve is consistent with previous literature[34] that revealed that (i) KaiB binding occurs over a shorter time span than KaiB unbinding and (ii) the duration of minimally bound KaiB (trough) is wider than the duration of maximally bound KaiB (peak) (Figure 5b, Figure S16, and Table S5). We note that a two-component model for describing FCS data is likely inappropriate as FCS is based on the translational diffusion time, which is in turn dependent on the molecular weights of various KaiABC complexes with various stoichiometries, and previous native mass spectrometry results[27] point toward this fact. On the other hand, for sufficiently large proteins where global rotational motion is slow, cw-EPR is dependent on only the local nitroxide tether and protein backbone motion. Thus, a two-component model is appropriate for $N19C_{3IAP}$ (Figure 3e).

DISCUSSION

Implications of cw-EPR Results for the Current Model of the Kai Oscillator. The discovery of $N19C_{3IAP}$ as a KaiB−KaiC interaction selective probe allowed binding kinetics to be observed in real time. The improved time resolution and theoretical support for selectivity offer an orthogonal window into the understanding of the Kai system.

Our cw-EPR and FA data suggest that the KaiB−$KaiC_{EE}$ interaction is weakly antagonized by KaiA transiently (Figure 4c,d). As pointed out above, the existence of more than two KaiB-containing species prevents interpretation of $K25C_{6IAF}$ FA as KaiB−KaiC binding when KaiA is present. Nevertheless, the consistency between these two techniques at differing labeling sites implies that this transient KaiA antagonization is unlikely to be a probe or technique-based artifact. The observed antagonization is surprising given that KaiA is known to be sequestered during the night state as a ternary KaiABC complex when S431 is phosphorylated.[20] As KaiA was observed to impact KaiB−KaiC binding in a phospho-state-dependent manner as determined by immunoprecipitation SDS−PAGE,[23] with an increasing level of KaiA leading to a nonlinear response in $KaiC_{pSpT}$−KaiB binding, the real-time observations presented in this study were not unreasonable. KaiA has been shown to act as a nucleotide exchange factor for KaiC,[18,19] the latter of which has only been crystallized in conjunction with KaiB in a post-ATP hydrolysis state.[21] We speculate that this transient KaiA-induced KaiBC antagonization is due to interactions between KaiA and A-loops on CII. This interaction weakens the CII ring integrity, which in turn weakens CII−CI ring stacking interactions.[13] As ring stacking stabilizes the posthydrolysis state of CI, weakened stacking promotes the prehydrolytic state of CI, which destabilizes KaiBC interactions. This antagonization occurs over 12 h, but the KaiBC population recovers on longer time scales as the spiked KaiA is sequestered into a KaiABC complex. This observation is consistent with exclusive activities of CI and CII rings that are reciprocally regulated.[23] Further experiments are necessary to evaluate the plausibility and molecular mechanism of this pathway and its relevance in clock resetting.

Limitations of cw-EPR as an Analytical Technique for Studying Protein−Protein Interactions. Prior to this work, SDSL−EPR has been used to determine the secondary structure[59] and oligomeric state[47] of membrane proteins as well as folding of both globular[60] and intrinsically disordered proteins.[53] Our current work illustrates that cw-EPR can be an analytical technique for studying protein−protein interactions in real time. However, there are two limitations that can limit the usefulness of cw-EPR in quantification and generalization to other systems to be discussed below.

(1) Site Design for Spin Labeling. Unlike FA where the fluorescence probe can be attached to surface residues or either terminus of the protein of interest,[50] the requirement for a change in the local environment (Figure 2c) for a corresponding spectral change in the nitroxide cw-EPR spectrum poses a unique problem. Researchers are often limited by existing crystal structures and biochemical intuition in designing mutants for probe conjugation while minimizing perturbations to biochemical reactivity. In this work, we showed that $N19C_{3IAP}$ was selective with respect to KaiB−KaiC interactions but the mutagenesis and labeling also enhanced KaiB's reactivity (Figure S2). SDSL is thus not necessarily a conservative mutation, and orthogonal functional assays should be employed to test the spin-labeled constructs' reactivity. Nevertheless, considering the potential of SDSL−EPR in resolving multiple species in real time by using magnetic field as the second abscissa, its application could be extended if this barrier in site design is lowered. We envision that future researchers should be able to design SDSL−EPR probe sites based on molecular dynamics (MD) simulations.[61−65] To that end, multiple strategies have been implemented to directly compute the cw-EPR spectra of spin-labeled proteins from MD simulations.[62−65] However, screening of multiple sites via a full MD simulation can be computationally demanding. Alternatively, rotamer libraries have previously been computed for multiple nitroxide spin-labels as coarse-grain approximations to the true dynamics of the nitroxide moiety to aid in designing probe sites for favorable distance measurements.[61,66] Computed within the rotamer library-based calculations are metrics such as nitroxide partition function Z, which measures the tightness of the site and root-mean-square deviation of the midpoint of the N−O group from the mean position, both of which might be correlated with nitroxide mobility. As only a single biologically active mutant was described in this work, there are insufficient data to correlate our results with MD or rotamer library predictions. Nevertheless, we anticipate that such a correlation can be established in the future with additional data and increasingly efficient schemes in computing nitroxide molecular dynamics.

(2) Sensitivity and Throughput. A second limitation to developing an SDSL−EPR-based biochemical assay is the limited sensitivity and throughput of cw-EPR. SDSL−cw-EPR at ambient temperatures has previously been performed with proteins at high concentrations[40] (~1 mM) to allow a sufficient S/N ratio. For practical biological assays, the protein concentration is often kept low to mimic physiological conditions and reduce the level of aggregation. This trade-off in sample concentration renders a low S/N ratio and ambiguity in spectral interpretation. In the context of the Kai clock, increasing the concentration of the Kai oscillator can lead to an increased level of ATP consumption and premature failure of the oscillator due to ATP depletion.[67] This contrasts with routine fluorescence assays in which nanomolar probe concentrations coupled with optical plate readers provide decent S/N ratios with high throughput. The S/N ratio

https://dx.doi.org/10.1021/acs.biochem.0c00279
Biochemistry 2020, 59, 2387−2400

limitation highlights the urgency for innovative detection schemes to improve cw-EPR sensitivity. In that respect, we anticipate that rapid-scan EPR[68] coupled with imaging[69] can satisfy both requirements of increased S/N ratio and throughput at physiological concentrations.

■ ASSOCIATED CONTENT

Supporting Information

The Supporting Information is available free of charge at https://pubs.acs.org/doi/10.1021/acs.biochem.0c00279.

Tables S1−S5, Figures S1−S16, and Supplementary Text (PDF)

Accession Codes

S. elongatus (PCC 7942) KaiC, UnitProt entry Q79PF4; *S. elongatus* (PCC 7942) KaiB, UnitProt entry Q79PF5; *S. elongatus* (PCC 7942) KaiA, UnitProt entry Q79PF6.

■ AUTHOR INFORMATION

Corresponding Authors

Andy LiWang − *School of Natural Sciences, Chemistry and Chemical Biology, Quantitative and Systems Biology, Health Sciences Research Institute, and Center for Cellular and Biomolecular Machines, University of California, Merced, California 95343, United States; Center for Circadian Biology, University of California, San Diego, La Jolla, California 92093, United States*; Phone: (209) 777-6341; Email: aliwang@ucmerced.edu

R. David Britt − *Department of Chemistry, University of California, Davis, California 95616, United States;* orcid.org/0000-0003-0889-8436; Phone: (530) 752-6377; Email: rdbritt@ucdavis.edu

Authors

Gary K. Chow − *Department of Chemistry, University of California, Davis, California 95616, United States;* orcid.org/0000-0001-9200-0857

Archana G. Chavan − *School of Natural Sciences, University of California, Merced, California 95343, United States*

Joel C. Heisler − *Chemistry and Chemical Biology, University of California, Merced, California 95343, United States*

Yong-Gang Chang − *School of Natural Sciences, University of California, Merced, California 95343, United States*

Complete contact information is available at: https://pubs.acs.org/10.1021/acs.biochem.0c00279

Funding

This work was supported by grants from the U.S. National Science Foundation (NSF-MCB-1615752 to R.D.B. and NSF-HRD-1547848 to CREST, the Center for Cellular and Biomolecular Machines at the University of California, Merced, CA), the National Institutes of Health (GM107521 to A.L.), and the Army Research Office (W911NF-17-1-0434 to A.L.).

Notes

The authors declare no competing financial interest.

■ ACKNOWLEDGMENTS

The authors thank Drs. William Jewell and Armann Andaya for their help in acquiring LCMS data. The authors thank Carrie L. Partch for valuable insights and G. Rao, L. Tao, A. R. Balo, and M. A. Nesbit for critical reading/helpful discussion.

■ REFERENCES

(1) Liu, Y., Tsinoremas, N. F., Johnson, C. H., Lebedeva, N. V., Golden, S. S., Ishiura, M., and Kondo, T. (1995) Circadian orchestration of gene expression in cyanobacteria. *Genes Dev. 9*, 1469−1478.

(2) Ouyang, Y., Andersson, C. R., Kondo, T., Golden, S. S., and Johnson, C. H. (1998) Resonating circadian clocks enhance fitness in cyanobacteria. *Proc. Natl. Acad. Sci. U. S. A. 95*, 8660−8664.

(3) Tomita, J., Nakajima, M., Kondo, T., and Iwasaki, H. (2005) No transcription-translation feedback in circadian rhythm of KaiC phosphorylation. *Science 307*, 251−254.

(4) Young, M. W., and Kay, S. A. (2001) Time zones: a comparative genetics of circadian clocks. *Nat. Rev. Genet. 2*, 702−715.

(5) Rust, M. J., Markson, J. S., Lane, W. S., Fisher, D. S., and O'Shea, E. K. (2007) Ordered phosphorylation governs oscillation of a three-protein circadian clock. *Science 318*, 809−812.

(6) Nishiwaki, T., Satomi, Y., Kitayama, Y., Terauchi, K., Kiyohara, R., Takao, T., and Kondo, T. (2007) A sequential program of dual phosphorylation of KaiC as a basis for circadian rhythm in cyanobacteria. *EMBO J. 26*, 4029−4037.

(7) Nakajima, M., Imai, K., Ito, H., Nishiwaki, T., Murayama, Y., Iwasaki, H., Oyama, T., and Kondo, T. (2005) Reconstitution of circadian oscillation of cyanobacterial KaiC phosphorylation in vitro. *Science 308*, 414−415.

(8) Wang, J. (2004) Nucleotide-dependent domain motions within rings of the RecA/AAA(+) superfamily. *J. Struct. Biol. 148*, 259−267.

(9) Phong, C., Markson, J. S., Wilhoite, C. M., and Rust, M. J. (2013) Robust and tunable circadian rhythms from differentially sensitive catalytic domains. *Proc. Natl. Acad. Sci. U. S. A. 110*, 1124−1129.

(10) Abe, J., Hiyama, T., Mukaiyama, A., Son, S., Mori, T., Saito, S., Osako, M., Wolanin, J., Yamashita, E., Kondo, T., and Akiyama, S. (2015) Atomic-scale origins of slowness in the cyanobacterial circadian clock. *Science 349*, 312−316.

(11) Murakami, R., Miyake, A., Iwase, R., Hayashi, F., Uzumaki, T., and Ishiura, M. (2008) ATPase activity and its temperature compensation of the cyanobacterial clock protein KaiC. *Genes Cells 13*, 387−395.

(12) Chang, Y. G., Kuo, N. W., Tseng, R., and LiWang, A. (2011) Flexibility of the C-terminal, or CII, ring of KaiC governs the rhythm of the circadian clock of cyanobacteria. *Proc. Natl. Acad. Sci. U. S. A. 108*, 14431−14436.

(13) Chang, Y. G., Tseng, R., Kuo, N. W., and LiWang, A. (2012) Rhythmic ring-ring stacking drives the circadian oscillator clockwise. *Proc. Natl. Acad. Sci. U. S. A. 109*, 16847−16851.

(14) Nishiwaki, T., and Kondo, T. (2012) Circadian autodephosphorylation of cyanobacterial clock protein KaiC occurs via formation of ATP as intermediate. *J. Biol. Chem. 287*, 18030−18035.

(15) Ye, S., Vakonakis, I., Ioerger, T. R., LiWang, A. C., and Sacchettini, J. C. (2004) Crystal structure of circadian clock protein KaiA from Synechococcus elongatus. *J. Biol. Chem. 279*, 20511−20518.

(16) Kim, Y. I., Dong, G., Carruthers, C. W., Golden, S. S., and LiWang, A. (2008) The day/night switch in KaiC, a central oscillator component of the circadian clock of cyanobacteria. *Proc. Natl. Acad. Sci. U. S. A. 105*, 12825−12830.

(17) Pattanayek, R., and Egli, M. (2015) Protein-Protein Interactions in the Cyanobacterial Circadian Clock: Structure of KaiA Dimer in Complex with C-Terminal KaiC Peptides at 2.8 angstrom Resolution. *Biochemistry 54*, 4575−4578.

(18) Nishiwaki-Ohkawa, T., Kitayama, Y., Ochiai, E., and Kondo, T. (2014) Exchange of ADP with ATP in the CII ATPase domain promotes autophosphorylation of cyanobacterial clock protein KaiC. *Proc. Natl. Acad. Sci. U. S. A. 111*, 4455−4460.

(19) Hong, L., Vani, B. P., Thiede, E. H., Rust, M. J., and Dinner, A. R. (2018) Molecular dynamics simulations of nucleotide release from the circadian clock protein KaiC reveal atomic-resolution functional insights. *Proc. Natl. Acad. Sci. U. S. A. 115*, E11475−E11484.

(20) Tseng, R., Chang, Y. G., Bravo, I., Latham, R., Chaudhary, A., Kuo, N. W., and LiWang, A. (2014) Cooperative KaiA-KaiB-KaiC interactions affect KaiB/SasA competition in the circadian clock of cyanobacteria. *J. Mol. Biol. 426*, 389−402.
(21) Tseng, R., Goularte, N. F., Chavan, A., Luu, J., Cohen, S. E., Chang, Y. G., Heisler, J., Li, S., Michael, A. K., Tripathi, S., Golden, S. S., LiWang, A., and Partch, C. L. (2017) Structural basis of the day-night transition in a bacterial circadian clock. *Science 355*, 1174−1180.
(22) Kitayama, Y., Iwasaki, H., Nishiwaki, T., and Kondo, T. (2003) KaiB functions as an attenuator of KaiC phosphorylation in the cyanobacterial circadian clock system. *EMBO J. 22*, 2127−2134.
(23) Lin, J., Chew, J., Chockanathan, U., and Rust, M. J. (2014) Mixtures of opposing phosphorylations within hexamers precisely time feedback in the cyanobacterial circadian clock. *Proc. Natl. Acad. Sci. U. S. A. 111*, E3937−E3945.
(24) Chang, Y. G., Cohen, S. E., Phong, C., Myers, W. K., Kim, Y. I., Tseng, R., Lin, J., Zhang, L., Boyd, J. S., Lee, Y., Kang, S., Lee, D., Li, S., Britt, R. D., Rust, M. J., Golden, S. S., and LiWang, A. (2015) A protein fold switch joins the circadian oscillator to clock output in cyanobacteria. *Science 349*, 324−328.
(25) Villarreal, S. A., Pattanayek, R., Williams, D. R., Mori, T., Qin, X. M., Johnson, C. H., Egli, M., and Stewart, P. L. (2013) CryoEM and Molecular Dynamics of the Circadian KaiB-KaiC Complex Indicates That KaiB Monomers Interact with KaiC and Block ATP Binding Clefts. *J. Mol. Biol. 425*, 3311−3324.
(26) Iwase, R., Imada, K., Hayashi, F., Uzumaki, T., Morishita, M., Onai, K., Furukawa, Y., Namba, K., and Ishiura, M. (2005) Functionally important substructures of circadian clock protein KaiB in a unique tetramer complex. *J. Biol. Chem. 280*, 43141−43149.
(27) Snijder, J., Burnley, R. J., Wiegard, A., Melquiond, A. S. J., Bonvin, A. M. J. J., Axmann, I. M., and Heck, A. J. R. (2014) Insight into cyanobacterial circadian timing from structural details of the KaiB-KaiC interaction. *Proc. Natl. Acad. Sci. U. S. A. 111*, 1379−1384.
(28) Snijder, J., Schuller, J., Wiegard, A., Lossl, P., Schmelling, N., Axmann, I., Plitzko, J., Forster, F., and Heck, A. (2017) Structures of the cyanobacterial circadian oscillator frozen in a fully assembled state. *Science 355*, 1181−1184.
(29) Chew, J., Leypunskiy, E., Lin, J., Murugan, A., and Rust, M. J. (2018) High protein copy number is required to suppress stochasticity in the cyanobacterial circadian clock. *Nat. Commun. 9*, 3004.
(30) Kitayama, Y., Nishiwaki-Ohkawa, T., Sugisawa, Y., and Kondo, T. (2013) KaiC intersubunit communication facilitates robustness of circadian rhythms in cyanobacteria. *Nat. Commun. 4*, 2897.
(31) van Zon, J. S., Lubensky, D. K., Altena, P. R., and ten Wolde, P. R. (2007) An allosteric model of circadian KaiC phosphorylation. *Proc. Natl. Acad. Sci. U. S. A. 104*, 7420−7425.
(32) Ito, H., Kageyama, H., Mutsuda, M., Nakajima, M., Oyama, T., and Kondo, T. (2007) Autonomous synchronization of the circadian KaiC phosphorylation rhythm. *Nat. Struct. Mol. Biol. 14*, 1084−1088.
(33) Emberly, E., and Wingreen, N. (2006) Hourglass model for a protein-based circadian oscillator. *Phys. Rev. Lett. 96*, 038303.
(34) Goda, K., Ito, H., Kondo, T., and Oyama, T. (2012) Fluorescence correlation spectroscopy to monitor Kai protein-based circadian oscillations in real time. *J. Biol. Chem. 287*, 3241−3248.
(35) Goda, K., Kondo, T., and Oyama, T. (2014) Effects of adenylates on the circadian interaction of KaiB with the KaiC complex in the reconstituted cyanobacterial Kai protein oscillator. *Biosci., Biotechnol., Biochem. 78*, 1833−1838.
(36) Heisler, J., Chavan, A., Chang, Y. G., and LiWang, A. (2019) Real-Time In Vitro Fluorescence Anisotropy of the Cyanobacterial Circadian Clock. *Methods Protoc. 2*, 42.
(37) Berliner, L. J., Ed. (1976) *Spin Labeling: Theory and Applications*, Academic Press, New York.
(38) Tyagarajan, K., Pretzer, E., and Wiktorowicz, J. E. (2003) Thiol-reactive dyes for fluorescence labeling of proteomic samples. *Electrophoresis 24*, 2348−2358.
(39) Zhang, Z., and Marshall, A. G. (1998) A universal algorithm for fast and automated charge state deconvolution of electrospray mass-to-charge ratio spectra. *J. Am. Soc. Mass Spectrom. 9*, 225−233.
(40) Zhang, Z., Fleissner, M. R., Tipikin, D. S., Liang, Z., Moscicki, J. K., Earle, K. A., Hubbell, W. L., and Freed, J. H. (2010) Multifrequency electron spin resonance study of the dynamics of spin labeled T4 lysozyme. *J. Phys. Chem. B 114*, 5503−5521.
(41) Eaton, G. R., Eaton, S. S., Barr, D. P., and Weber, R. T. (2010) *Quantitative EPR: A Practitioners Guide*, Springer, Vienna.
(42) Stoll, S., and Schweiger, A. (2006) Easy Spin, a comprehensive software package for spectral simulation and analysis in EPR. *J. Magn. Reson. 178*, 42−55.
(43) Czoch, R. (1996) Quantitative EPR — Sensitivity to experimental conditions and optimal setting of recording parameters. *Appl. Magn. Reson. 10*, 293−317.
(44) Edwards, K. D., Akman, O. E., Knox, K., Lumsden, P. J., Thomson, A. W., Brown, P. E., Pokhilko, A., Kozma-Bognar, L., Nagy, F., Rand, D. A., and Millar, A. J. (2010) Quantitative analysis of regulatory flexibility under changing environmental conditions. *Mol. Syst. Biol. 6*, 424.
(45) Barrodale, I., and Erickson, R. E. (1980) Algorithms for least-squares linear prediction and maximum entropy spectral analysis—Part I: Theory. *Geophysics 45*, 420−432.
(46) Lomb, N. R. (1976) Least-squares frequency analysis of unequally spaced data. *Astrophys. Space Sci. 39*, 447−462.
(47) Langen, R., Isas, J. M., Luecke, H., Haigler, H. T., and Hubbell, W. L. (1998) Membrane-mediated assembly of annexins studied by site-directed spin labeling. *J. Biol. Chem. 273*, 22453−22457.
(48) Altenbach, C., Oh, K. J., Trabanino, R. J., Hideg, K., and Hubbell, W. L. (2001) Estimation of inter-residue distances in spin labeled proteins at physiological temperatures: experimental strategies and practical limitations. *Biochemistry 40*, 15471−15482.
(49) Halle, B., and Davidovic, M. (2003) Biomolecular hydration: from water dynamics to hydrodynamics. *Proc. Natl. Acad. Sci. U. S. A. 100*, 12135−12140.
(50) Moerke, N. J. (2009) Fluorescence Polarization (FP) Assays for Monitoring Peptide-Protein or Nucleic Acid−Protein Binding. *Curr. Protoc. Chem. Biol. 1*, 1−15.
(51) Mutoh, R., Mino, H., Murakami, R., Uzumaki, T., Takabayashi, A., Ishii, K., and Ishiura, M. (2010) Direct interaction between KaiA and KaiB revealed by a site-directed spin labeling electron spin resonance analysis. *Genes Cells 15*, 269−280.
(52) Erales, J., Lorenzi, M., Lebrun, R., Fournel, A., Etienne, E., Courcelle, C., Guigliarelli, B., Gontero, B., and Belle, V. (2009) A new function of GAPDH from Chlamydomonas reinhardtii: a thiol-disulfide exchange reaction with CP12. *Biochemistry 48*, 6034−6040.
(53) Pirman, N. L., Milshteyn, E., Galiano, L., Hewlett, J. C., and Fanucci, G. E. (2011) Characterization of the disordered-to-α-helical transition of IA_3 by SDSL-EPR spectroscopy. *Protein Sci. 20*, 150−159.
(54) Fontaine, S. D., Reid, R., Robinson, L., Ashley, G. W., and Santi, D. V. (2015) Long-term stabilization of maleimide-thiol conjugates. *Bioconjugate Chem. 26*, 145−152.
(55) Mutoh, R., Mino, H., Murakami, R., Uzumaki, T., and Ishiura, M. (2011) Thermodynamically Induced Conformational Changes of the Cyanobacterial Circadian Clock Protein KaiB. *Appl. Magn. Reson. 40*, 525−534.
(56) Murakami, R., Yunoki, Y., Ishii, K., Terauchi, K., Uchiyama, S., Yagi, H., and Kato, K. (2019) Cooperative Binding of KaiB to the KaiC Hexamer Ensures Accurate Circadian Clock Oscillation in Cyanobacteria. *Int. J. Mol. Sci. 20*, 4550.
(57) Song, L., Liu, Z., Kaur, P., Esquiaqui, J. M., Hunter, R. I., Hill, S., Smith, G. M., and Fanucci, G. E. (2016) Toward increased concentration sensitivity for continuous wave EPR investigations of spin-labeled biological macromolecules at high fields. *J. Magn. Reson. 265*, 188−196.
(58) Wax, M., and Kailath, T. (1985) Detection of signals by information theoretic criteria. *IEEE Trans. Acoust., Speech, Signal Process. 33*, 387−392.

https://dx.doi.org/10.1021/acs.biochem.0c00279
Biochemistry 2020, 59, 2387−2400

(59) Altenbach, C., Yang, K., Farrens, D. L., Farahbakhsh, Z. T., Khorana, H. G., and Hubbell, W. L. (1996) Structural features and light-dependent changes in the cytoplasmic interhelical E-F loop region of rhodopsin: a site-directed spin-labeling study. *Biochemistry 35*, 12470−12478.
(60) Hubbell, W. L., Mchaourab, H. S., Altenbach, C., and Lietzow, M. A. (1996) Watching proteins move using site-directed spin labeling. *Structure 4*, 779−783.
(61) Polyhach, Y., Bordignon, E., and Jeschke, G. (2011) Rotamer libraries of spin labelled cysteines for protein studies. *Phys. Chem. Chem. Phys. 13*, 2356−2366.
(62) DeSensi, S. C., Rangel, D. P., Beth, A. H., Lybrand, T. P., and Hustedt, E. J. (2008) Simulation of nitroxide electron paramagnetic resonance spectra from brownian trajectories and molecular dynamics simulations. *Biophys. J. 94*, 3798−3809.
(63) Martin, P. D., Svensson, B., Thomas, D. D., and Stoll, S. (2019) Trajectory-Based Simulation of EPR Spectra: Models of Rotational Motion for Spin Labels on Proteins. *J. Phys. Chem. B 123*, 10131−10141.
(64) Budil, D. E., Sale, K. L., Khairy, K. A., and Fajer, P. G. (2006) Calculating slow-motional electron paramagnetic resonance spectra from molecular dynamics using a diffusion operator approach. *J. Phys. Chem. A 110*, 3703−3713.
(65) Robinson, B. H., Slutsky, L. J., and Auteri, F. P. (1992) Direct simulation of continuous wave electron paramagnetic resonance spectra from Brownian dynamics trajectories. *J. Chem. Phys. 96*, 2609−2616.
(66) Jeschke, G. (2018) MMM: A toolbox for integrative structure modeling. *Protein Sci. 27*, 76−85.
(67) Terauchi, K., Kitayama, Y., Nishiwaki, T., Miwa, K., Murayama, Y., Oyama, T., and Kondo, T. (2007) ATPase activity of KaiC determines the basic timing for circadian clock of cyanobacteria. *Proc. Natl. Acad. Sci. U. S. A. 104*, 16377−16381.
(68) Mitchell, D. G., Rosen, G. M., Tseitlin, M., Symmes, B., Eaton, S. S., and Eaton, G. R. (2013) Use of rapid-scan EPR to improve detection sensitivity for spin-trapped radicals. *Biophys. J. 105*, 338−342.
(69) Eaton, S. S., Shi, Y., Woodcock, L., Buchanan, L. A., McPeak, J., Quine, R. W., Rinard, G. A., Epel, B., Halpern, H. J., and Eaton, G. R. (2017) Rapid-scan EPR imaging. *J. Magn. Reson. 280*, 140−148.

https://dx.doi.org/10.1021/acs.biochem.0c00279
Biochemistry 2020, 59, 2387−2400

Supporting Information for

Monitoring Protein-Protein Interactions in the Cyanobacterial Circadian Clock in Real Time via Electron Paramagnetic Resonance Spectroscopy

Gary K. Chow,[†] Archana G. Chavan,[‡] Joel Heisler,[§] Yong-Gang Chang,[‡,^] Andy LiWang,[*,‡,§,∥,⊥,#,□] R. David Britt[*,†]

[†]Department of Chemistry, University of California, Davis, CA 95616

[‡]School of Natural Sciences, [§]Chemistry and Chemical Biology, [∥] Quantitative and Systems Biology, [⊥]Health Sciences Research Institute, and [#]Center for Cellular and Biomolecular Machines, University of California, Merced, CA 95343

[□]Center for Circadian Biology, University of California, San Diego, La Jolla, CA 92093.

Corresponding Authors

*Andy LiWang – Email: aliwang@ucmerced.edu. Phone: (209) 777-6341.

*R. David Britt – Email: rdbritt@ucdavis.edu. Phone: (530) 752-6377.

Present address

^Y.G.C.: Monash Biomedicine Discovery Institute, Monash University, Clayton VIC, 3800, Australia.

CONTENTS

PROTEIN QUALITY CONTROL

Figure S1. Intact LCMS of $N19C_{3IAP}$ demonstrates complete spin labelling

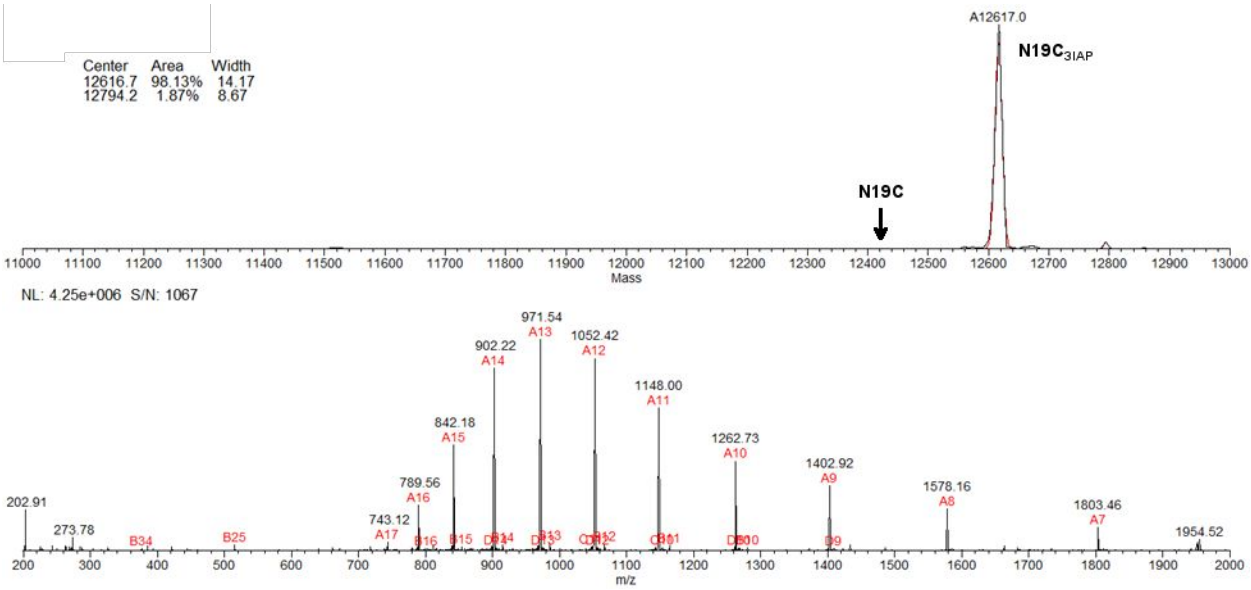

Top: transformed spectrum. Bottom: raw spectrum. LCMS masses: $N19C_{3IAP}$ (Calc: 12617.68; Found: 12617.0).

Figure S2. Native-PAGE of WT-KaiB and $N19C_{3IAP}$ binding to $KaiC_{EE}$.

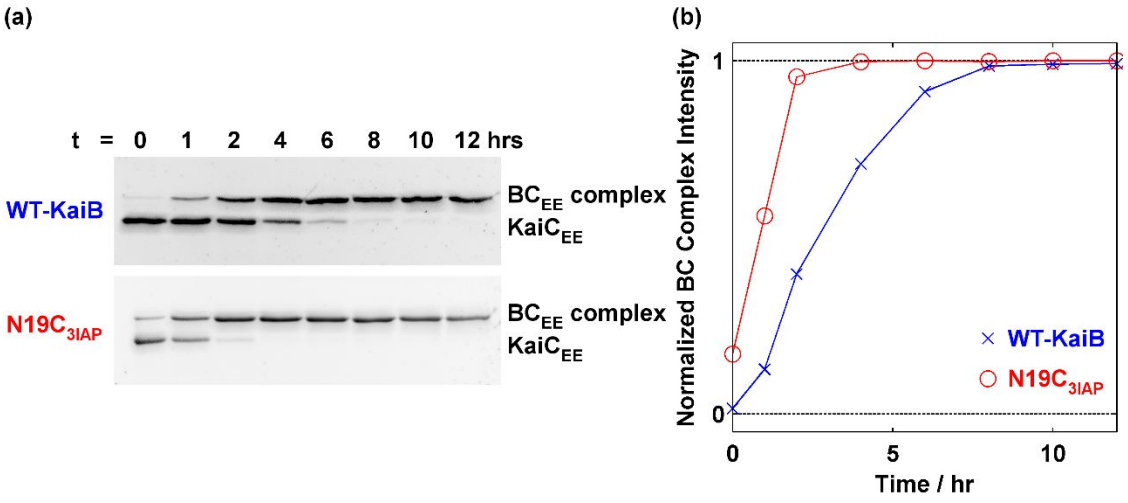

(a) Native-PAGE of samples collected at various time points from initial mixing of KaiB and $KaiC_{EE}$ as indicated on top of the images. Only KaiC-containing bands are shown. Species assignment is shown on the right. (b) KaiB-$KaiC_{EE}$ complexation estimated by densitometry. Traces refer to WT-KaiB (blue crosses) and $N19C_{3IAP}$ (red circles).

Figure S3. Fluorescence anisotropy assay on functionality of $N19C_{3IAP}$ in the in vitro oscillator reaction.

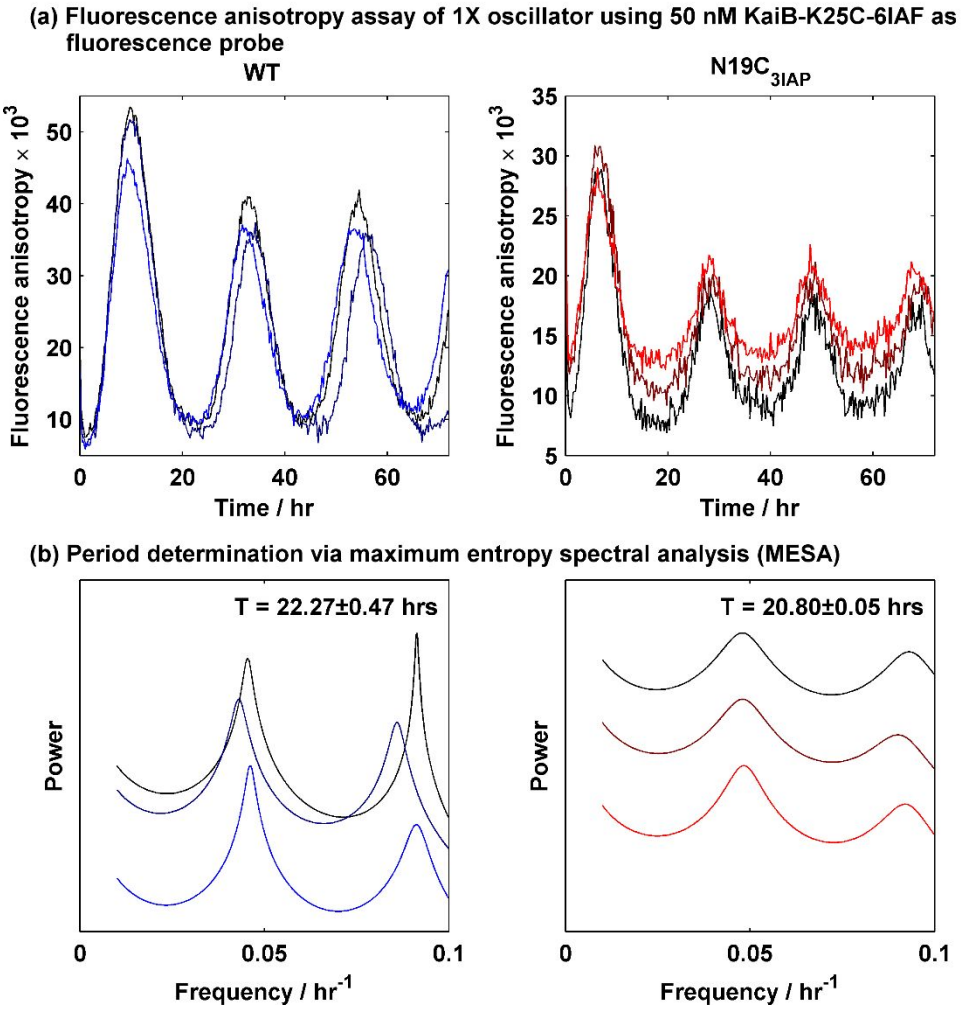

(a) Real-time fluorescence anisotropy traces of 1X oscillator reactions using WT-KaiB (blue) and $N19C_{3IAP}$ (red). In each plot, the three traces of varying brightness show results from technical triplicates. (b) Corresponding periodograms computed using maximum entropy spectral analysis (MESA) with the mean and SEM of the periods shown (n = 3).

EPR DATA PREPROCESSING

Figure S4. Microwave frequency drift correction.

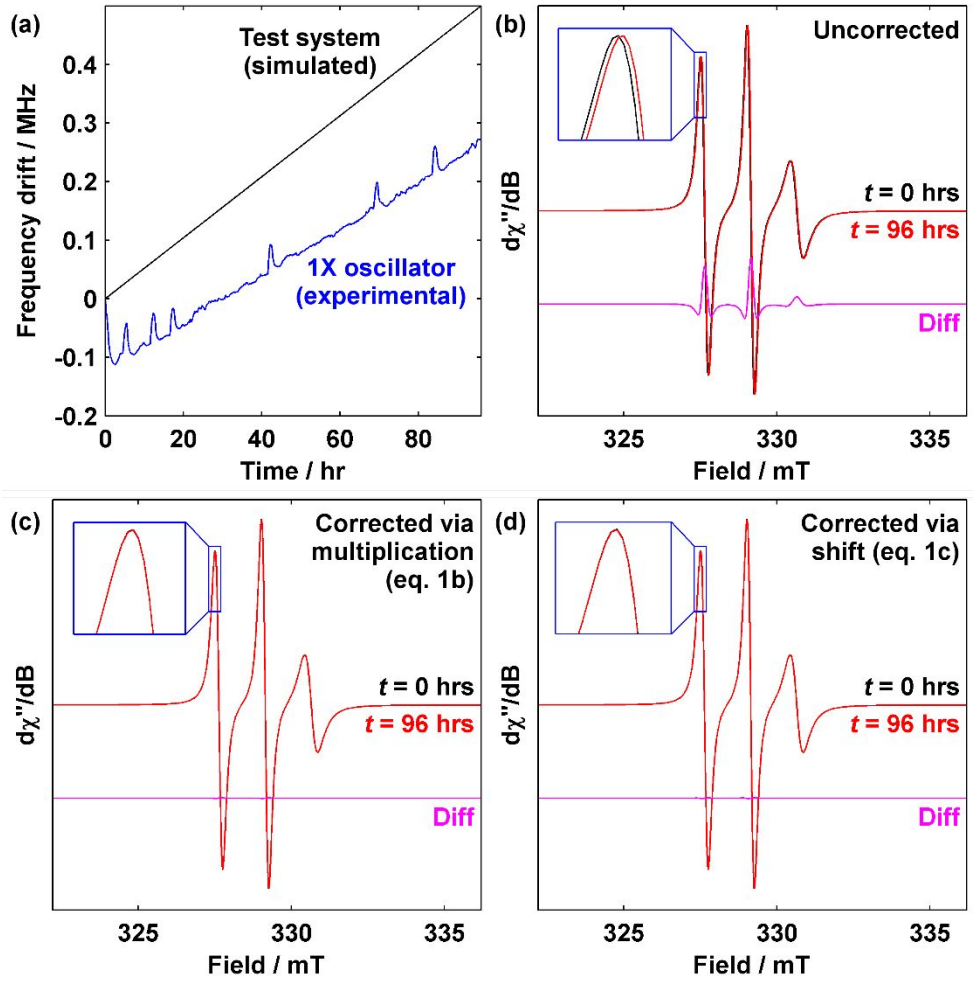

(a) Frequency drift plot of idealized test system (black) and experimental frequency drift observed in 1X $N19C_{3IAP}$ oscillator (blue). (b) Effect of microwave frequency drift on simulated spectrum at the beginning (black) and end (red) of the experiment. The difference spectrum is shown in magenta. See Table S1 for simulation details. (c) and (d) Demonstration of effectiveness of drift correction via multiplication (eq. 1b) or shift (eq. 1c) with identical coloring schemes as (b). Insets in (b)-(d) show zoomed in view of the boxed region.

Figure S5. Background correction.

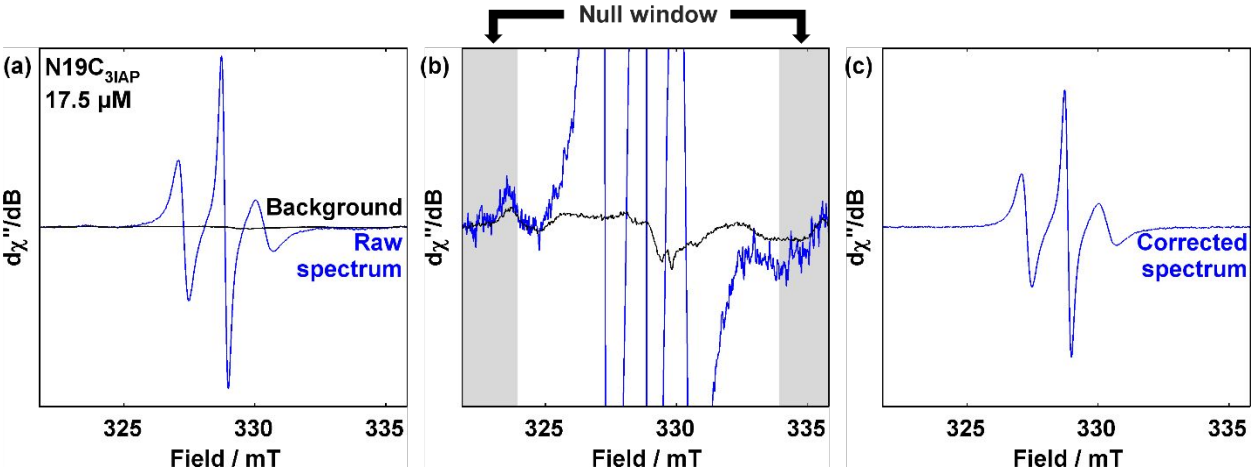

(a) Comparison of raw spectrum of $N19C_{3IAP}$ (blue) overlaid with background (black). (b) Expanded view of (a) to show the structure of the background signal showing trace manganese signals from the resonator cavity. Shaded area shows null window used in determining the magnitude of background necessary for background correction. (c) Background corrected spectrum.

Figure S6. Observation and evaluation of impact of time-dependent "*B*-shift".

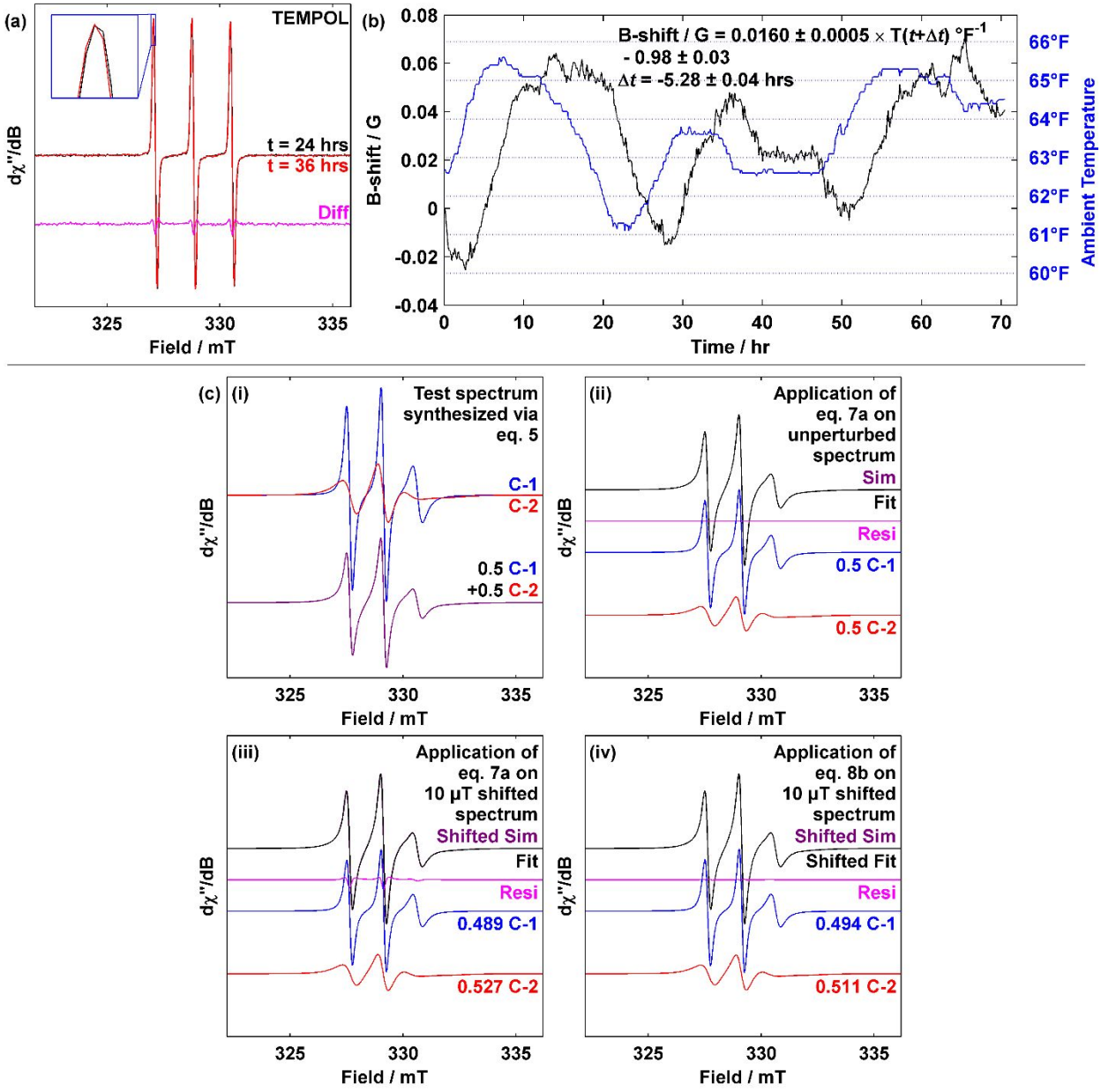

(a) cw-EPR spectrum of TEMPOL (20 μM) collected at 24 (black) and 36 (red) hrs after beginning acquisition. The difference is shown in magenta. (b) Plot of experimental "*B*-shift" (black) and variations in ambient temperature (blue) over 3 days. (c) Evaluation of the effect of "*B*-shift" on ratiometric spin quantification. (i) Motional components C-1 (τ_c = 1 ns, blue) and C-2 (τ_c = 3.16 ns, red) and synthesized spectrum using their weighted sum (purple). (ii) Solving for

weights of C-1 and C-2 via linear regression (eq. 7a) and the resultant spectrum (black) overlaid on synthesized spectrum in (i). (iii) Solving for weights of C-1 and C-2 via linear regression (eq. 7a) on the synthesized spectrum in (i) that has been shifted by 10 μT. (iv) Solving for weights of C-1 and C-2 via nonlinear regression with simultaneous fitting of "*B*-shift" (eq. 8b) on the synthesized spectrum in (i) that has been shifted by 10 μT. Residuals in (ii)-(iv) are shown in magenta.

QUALITATIVE EPR SPECTRAL FITTING

Table S1. Parameters used in illustrating the effect of motion on nitroxide cw-EPR spectra.

	Figure	g	A / MHz	$\log_{10}(\tau_c/\mathrm{ns})$	Phenomenological linewidth (Gaussian/Lorentzian) / MHz
Test System	2b	[2.0086, 2.0060, 2.0023]	[12, 16, 100]	-11	[0, 0.05]
				-10	
	2b, S4, S6			-9	
	2b, S6			-8.5	
				-8	
	2b			-7.5	
				-7	
				Rigid limit	[0.2, 0.2]

Microwave frequency was set to 9.24 GHz and simulated spectra were modulated at 0.19 mT to emulate experimental conditions.

Figure S7. Stacked plot of $N19C_{3IAP}$-$KaiC_{EE}$ reaction spectra.

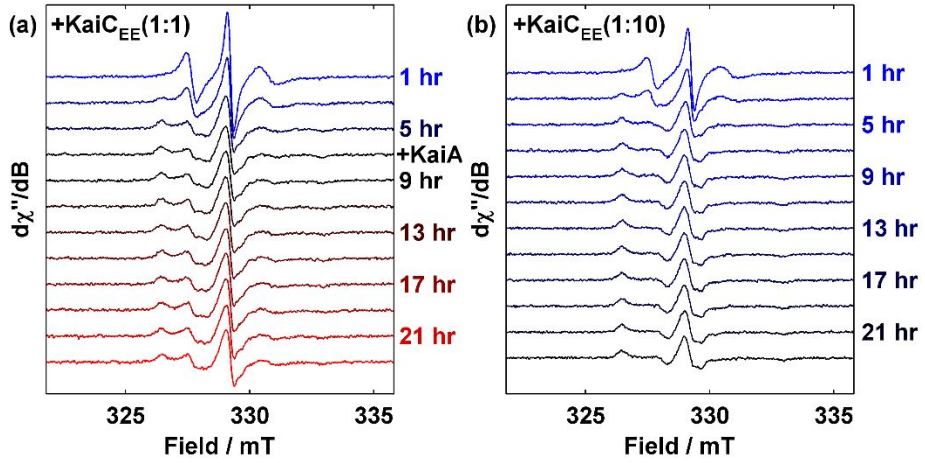

Reactions were performed with $N19C_{3IAP}$-$KaiC_{EE}$ ratios of (a) 1:1 and (b) 1:10 respectively using 17.5 μM $N19C_{3IAP}$. Spectra shown above are background corrected. In (a), KaiA was spiked at *t* = 7 hrs.

Figure S8. Fitting of $N19C_{3IAP}$-$KaiC_{EE}$ reaction spectra using slow-motion nitroxide spin model.

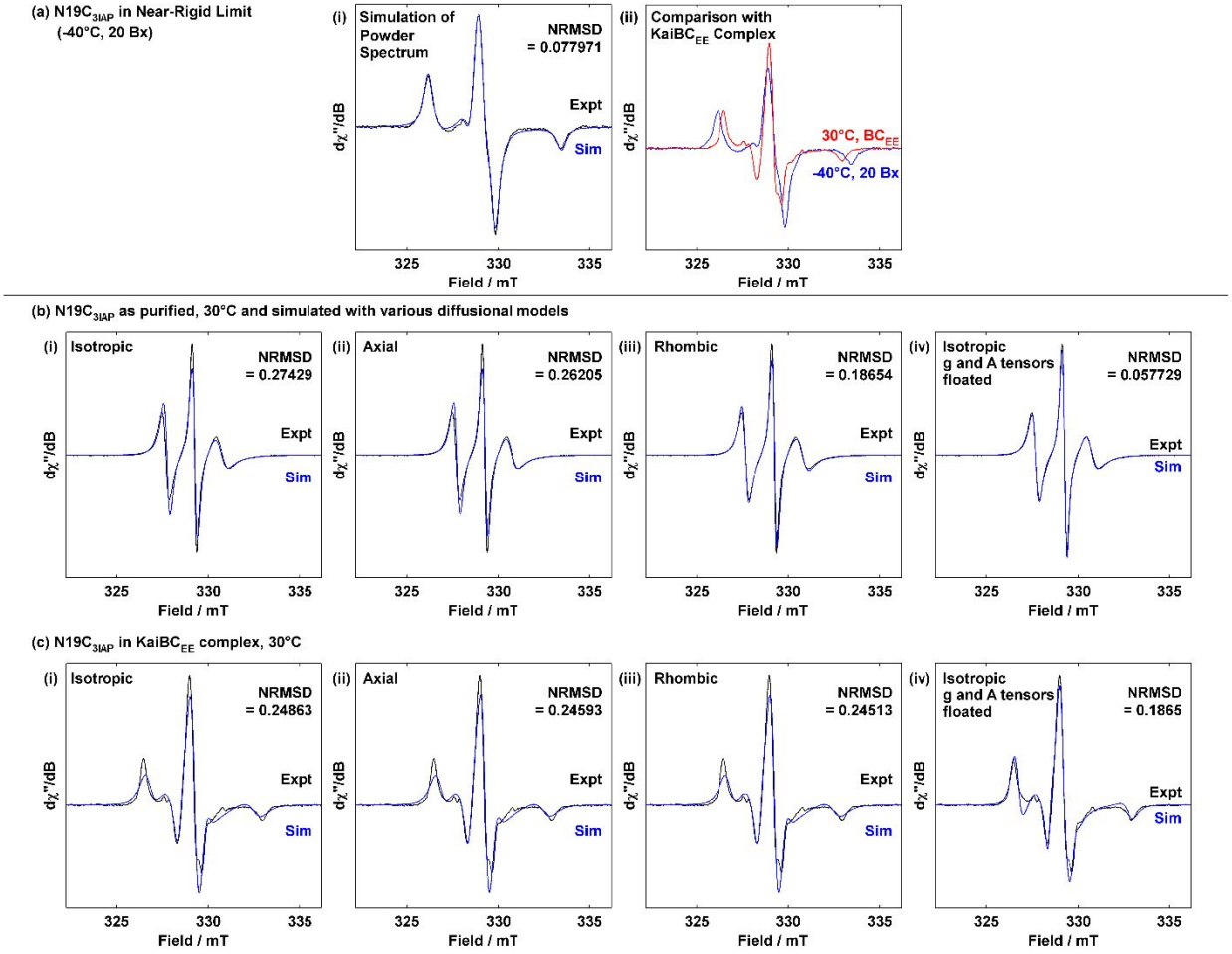

(a) cw-EPR spectrum of $N19C_{3IAP}$ at -40°C with 20% w/w sucrose (20 Bx) with (i) its simulations and (ii) in comparison with $KaiC_{EE}$-bound $N19C_{3IAP}$ shows that the latter is not in the solid-state regime. (b) and (c) Comparison of experimental and simulated spectra for free and KaiC-bound $N19C_{3IAP}$ respectively using (i) isotropic, (ii) axial and (iii) rhombic rotational diffusion models, and (iv) isotropic rotational diffusion while floating *g* and *A* tensors away from their rigid limit values. Refer to Table S2 for simulation parameters.

Table S2. Summary of spin parameters determined by least squares fitting of experimental $N19C_{3IAP}$ spectra.

g and *A* are listed in the order of *xx*, *yy* and *zz*. For τ_c, axial values are listed in the order of τ_{xy} and τ_z whereas rhombic values are listed in the order of τ_x, τ_y and τ_z. Square brackets indicate magnetic field bootstrap estimated 95% CI, $n_{bootstrap} = 200$.

N19C$_{3IAP}$		**Figure**	***g***	***A* / MHz**	**τ_c^{expt} / ns**	**Lw / mT***	**NRMSD**
Near-rigid Limit (20Bx, 233K)		S8a	2.0082, 2.0063, 2.00232; [2.0080, 2.0084], [2.0062, 2.0064], [2.00228, 2.00239]	17.1, 11.7, 102.28; [16.1, 18.6], [9.9, 13.3], [102.03, 102.48]	-	0.21, 0.28; [0.18, 0.30], [0.26, 0.30]	0.078
***g*, *A* fixed**	KaiB	S8bi			1.9; [1.8, 2.1]	-	0.274
		S8bii			1.8, $10^{5\#}$; [1.7, 2.0], [#]	-	0.262
		3f, S8biii			2.6, 1.1, $10^{5\#}$; [2.5, 2.7], [1.0, 1.2], [#]	-	0.187
	Kai(A)BC	S8ci			7.7; [7.3, 8.2]	-	0.249
		S8cii			7.8, 3.2; [7.2, 8.2], [2.0, 5.4]	-	0.246
		3f, S8ciii			7.0, 9.1, 3.6; [6.5, 7.3], [7.8, 10.3], [2.2, 6.3]	-	0.245
***g*, *A* floated**	KaiB	S8biv	2.0067, 2.0067, 2.0039	30, 15, 88	3.2	-	0.058
	Kai(A)BC	S8civ	2.0078, 2.0074, 2.0021	19, 13, 100	15.4	-	0.187

* Phenomenological Gaussian and Lorentzian peak-to-peak linewidths in mT.

Poorly constrained (reached lower or upper bound of parameter search space).

Table S3. Rotational correlation time estimated by Stokes-Einstein relation.

Structure (PDB)		**Monomeric fs-KaiB (5JWR)**	**Tetrameric gs-KaiB (4KSO)**	**KaiC-bound Kai-B (5JWQ)**
Approximate Shape and Dimension / nm		Sphere $r = 1.6$	Oblong	Cube $l = 10$
Molecular mass / g mol^{-1} (*)		11436	45745	413848
Approximate Volume / nm^3	Crystal structure	17.2	≈ 17.2 × 4 = 68.8	1000
	Specific volume	13.9	55.5	501.8
Stokes-Einstein Estimated τ_c (τ_c^{SE}) at 303 K / ns	Crystal structure	3.27	13.1	191
	Specific volume	2.64	10.6	95.7
Experimental N19C$_{3IAP}$ τ_c ($\tau_{c,iso}^{expt}$) / ns		-	1.9; [1.8, 2.1]	7.7; [7.3, 8.2]

* Wildtype sequences were used to calculate molecular mass.

Figure S9. Detection of KaiA-N19C$_{3IAP}$ interactions and spectral simulations.

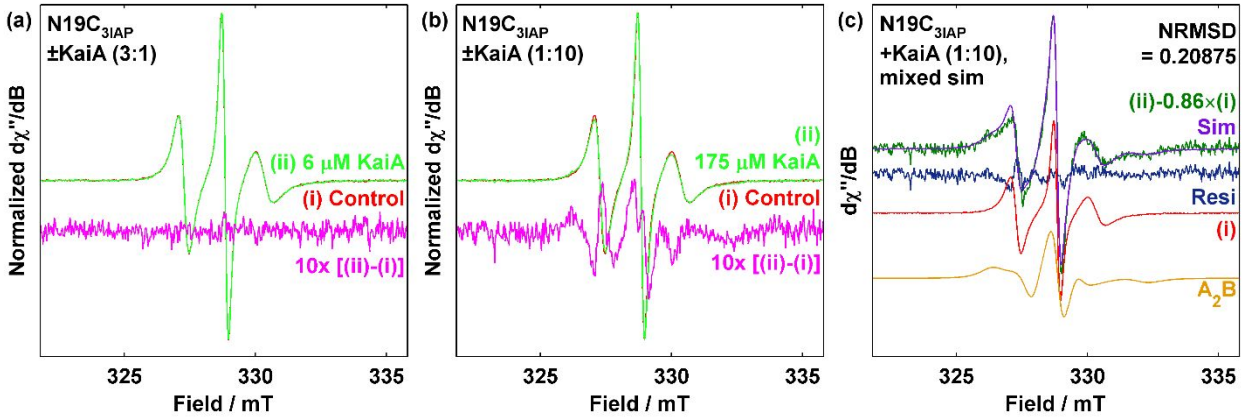

(a) and (b) comparison of cw-EPR spectra acquired with 17.5 μM N19C$_{3IAP}$ (red) against N19C$_{3IAP}$ equilibrated with 6 μM (a) and 175 μM (b) KaiA (light green). Spectra were normalized by their maximum intensity. The difference is shown in magenta below. (c) Semiphenomenological fitting (purple) of subtraction spectrum (green) obtained from (b) to a sum of free N19C$_{3IAP}$ (red) and KaiA$_2$B complex (orange). Residual is shown in dark blue. Refer to Table S4 for simulation parameters.

Table S4. Estimation of KaiB-KaiA direct binding dissociation constant.

Spectral changes were observed when $N19C_{3IAP}$ was equilibrated with tenfold excess KaiA. The new species was assumed to be A_2B and its quantity was estimated via spectral subtraction and simulation. The *g* and *A* values were fixed from Table S2 whereas isotropic τ_c and weight were floated. Square brackets indicate magnetic field bootstrap estimated 95% CI, $n_{bootstrap} = 200$.

$N19C_{3IAP}$ + 10x KaiA (A_2B)	**Figure**	**τ_c^{expt} / ns**	**Weight in subtraction spectrum / %**	**Weight in original spectrum / %**	**K_D^{app} / mM[#]**	**NRMSD**
	S9c	5.3 [4.6, 6.2]	56 [53, 59]	7.8 [7.4, 8.2]	1.0 [0.96, 1.1]	0.209

* Magnetic field bootstrapping produced a narrow distribution of best fit values likely because the parameter set entered a local minimum in the search space.

[#] Estimated by assuming the reaction

$$A_2 + B \rightleftharpoons A_2B; K_D^{app} = \frac{[A_2][B]}{[A_2B]}$$

without accounting for KaiB tetramer-monomer equilibrium, $[B]_0 = 17.5$ μM and $[A_2]_0 = 87.5$ μM. This calculation is only performed as a rough estimate of the KaiA-KaiB interaction strength. Note that the subtraction-simulation-quantification procedure places a lower limit on the fraction of A_2B and consequently an upper limit of K_D^{app}. See Supplementary Text for details.

QUANTITATIVE CW-EPR FITTING BASED KINETICS

Figure S10. Determination of scaling factor between B_{free} and B_{bound}.

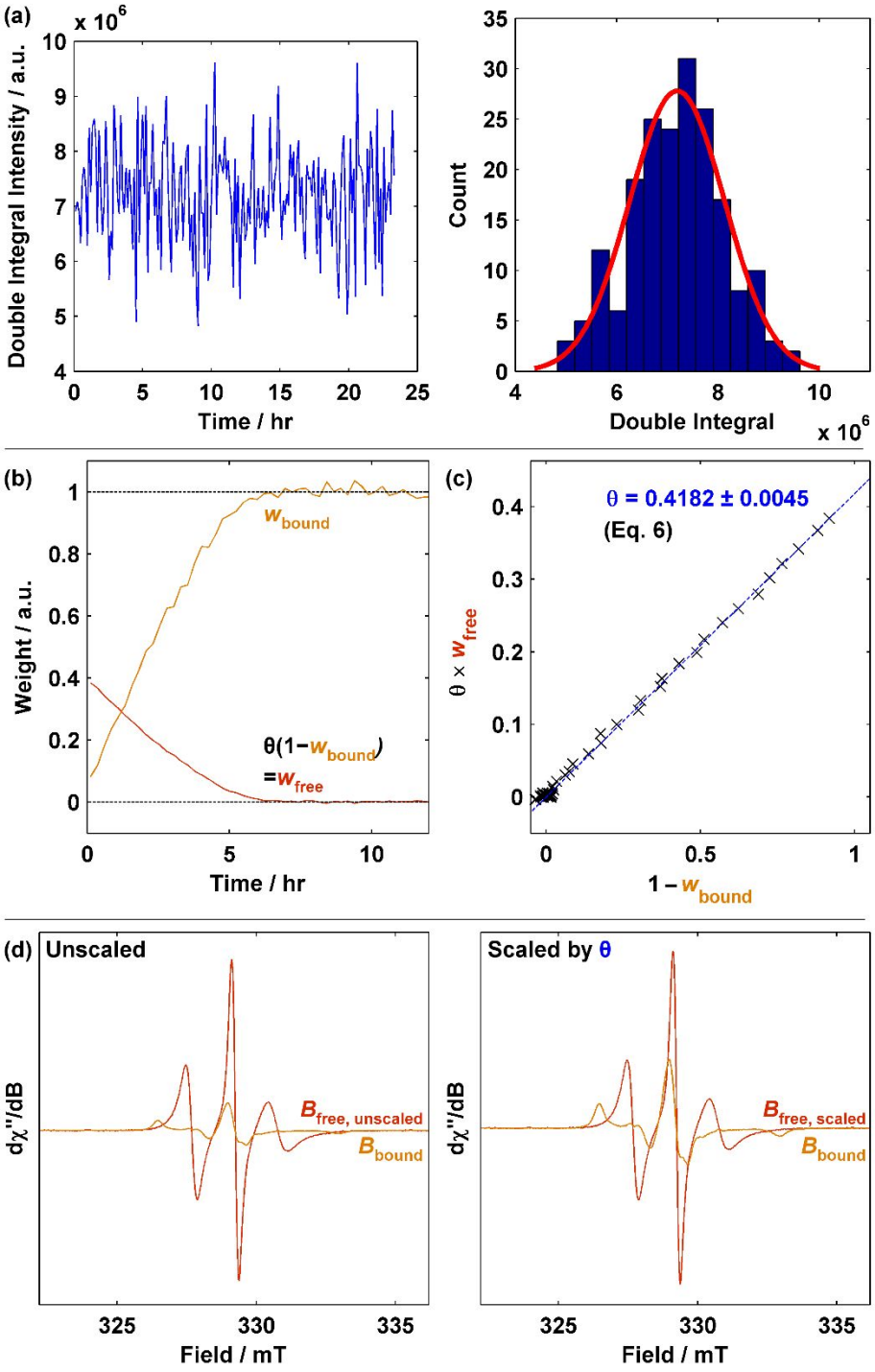

$N19C_{3IAP}$ was incubated with tenfold $KaiC_{EE}$ and cw-EPR spectra were collected over 24 hours. (a) Normalization of spectra via double integral is prone to noise and baseline induced errors. Left: time dependence of numerical double integral. Right: histogram and fit to Gaussian distribution of numerical double integral. (b) Fitting of weights without spectral scaling produces non-unity sums of weights. (c) Plot of weights of free KaiB against KaiC-bound KaiB weights. The error in θ shows 95% CI from linear regression. (d) Plot of unscaled (left) and scaled (right) spectra used for quantification of KaiC-bound KaiB. For (b) and (d), free KaiB is shown in red whereas KaiC-bound KaiB is shown in orange.

Figure S11. Quantitative $N19C_{3IAP}$-$KaiC_{EE}$ binding at 5X protein concentrations.

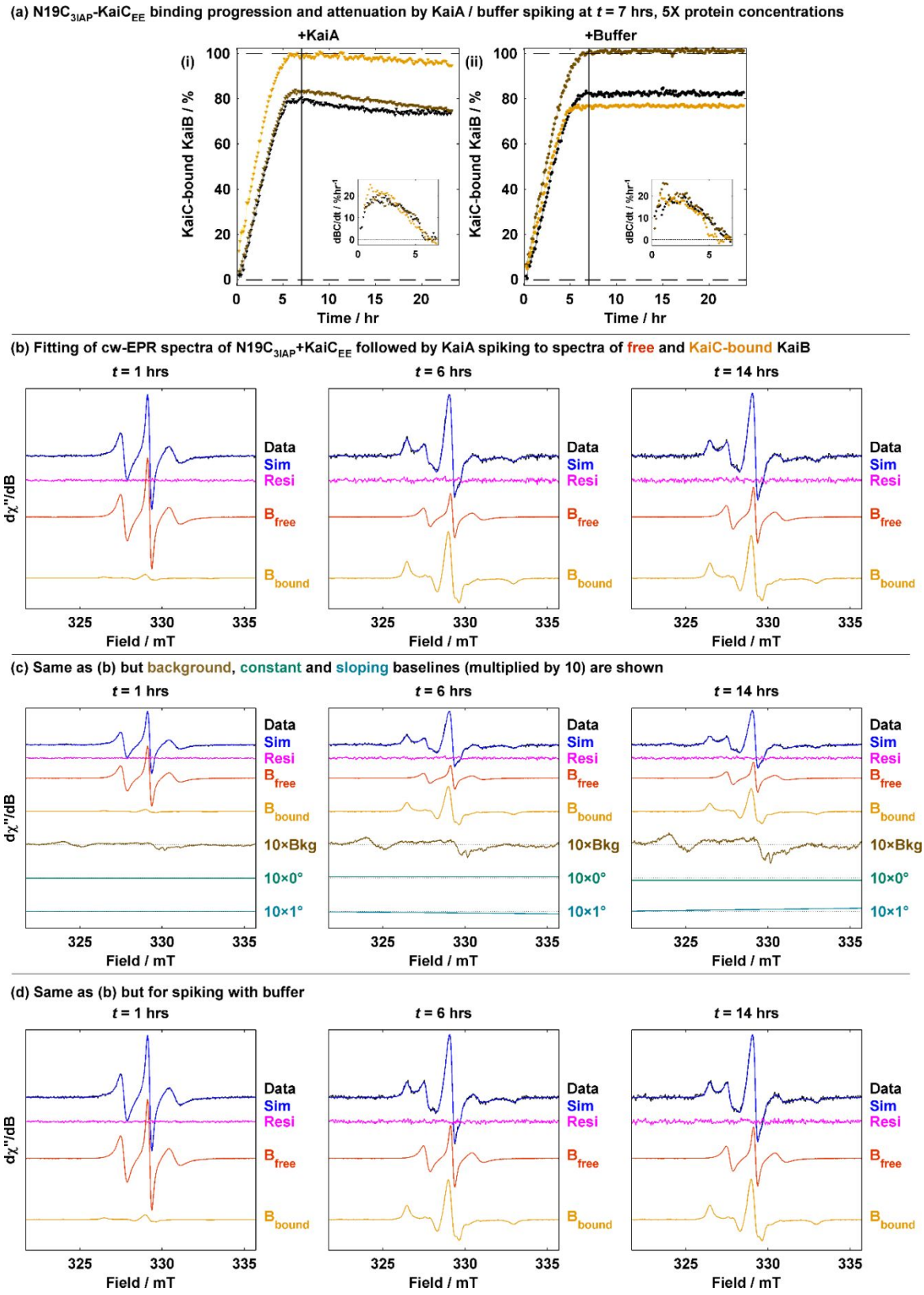

Kinetics and fitting of 5X $KaiC_{EE}$ phosphomimetic reaction with $N19C_{3IAP}$ at 1:1 stoichiometry followed by spiking with KaiA or buffer at $t \sim 7$ hrs. (a) Binding progression curve of triplicates of addition with KaiA (left) or buffer (right). Insets show binding velocity of corresponding experiments via Savitzky-Golay smoothing with 7-point window and 2nd order polynomials prior spiking. (b) Fitting of spectra for one replicate of KaiA spiking (brown trace in ai) using standard spectra of $N19C_{3IAP}$ and $N19C_{3IAP}$ in a tenfold excess of $KaiBC_{EE}$ at selected timepoints. Background and baseline components have been subtracted from both experimental and simulated data. (c) Same as (b) but background (brown) and baseline (constant / 0°, turquoise and linear / 1°, light blue) components are shown and multiplied by a factor of ten. (d) Same as (b) but buffer was spiked instead (black trace in aii).

Figure S12. Quantitative $N19C_{3IAP}$-$KaiC_{EE}$ binding at 1X protein concentrations.

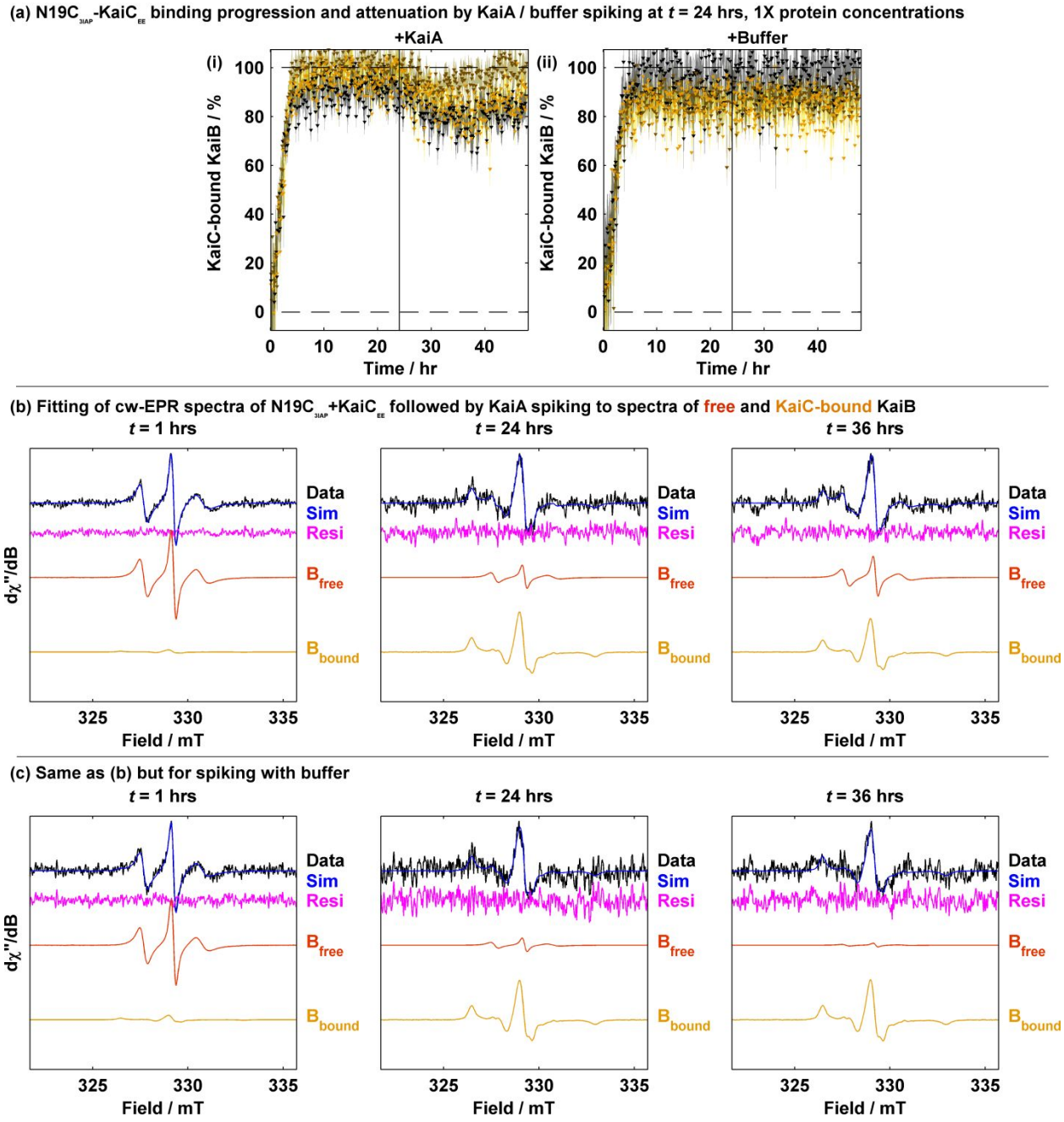

Kinetics and fitting of 1X $KaiC_{EE}$ phosphomimetic reaction with $N19C_{3IAP}$ at 1:1 stoichiometry followed by spiking with KaiA or buffer at $t \sim 24$ hrs. (a) Binding progression curve of triplicates of addition with KaiA (left) or buffer (right). (b) Fitting of spectra for one replicate of KaiA spiking (black trace in ai) using standard spectra of $N19C_{3IAP}$ and $N19C_{3IAP}$ in a tenfold excess of

$KaiBC_{EE}$ at selected timepoints. Background and baseline components have been subtracted from both experimental and simulated data. (c) Same as (b) but buffer was spiked instead (black trace in aii).

Figure S13. Raw data of fluorescence anisotropy based KaiB-KaiC$_{EE}$ binding assay.

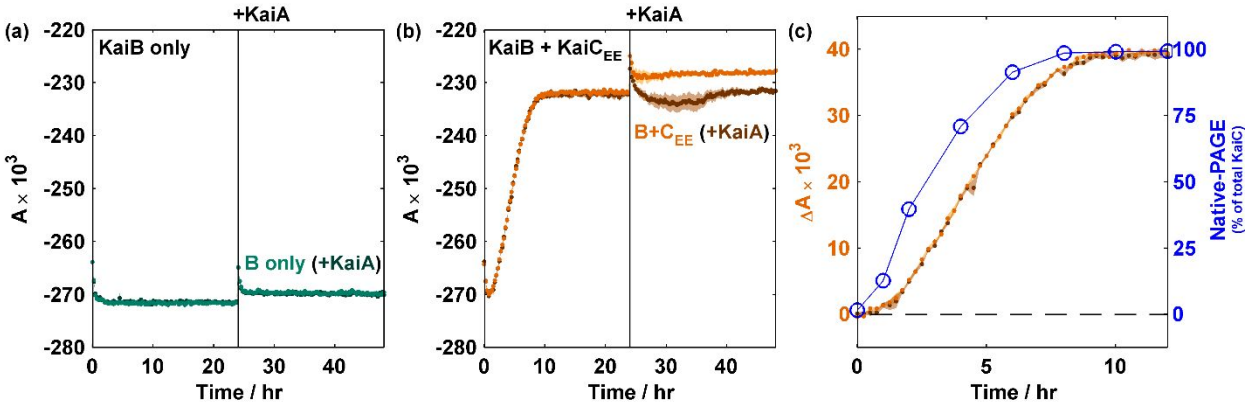

Fluorescence anisotropy of KaiB-K25C-6IAF (K25C$_{6IAF}$, 50 nM) in 3.45 μM WT-KaiB in the absence (a, turquoise) and presence (b, orange) of KaiC$_{EE}$, 3.5 μM. Shaded areas show SEM (n = 3). Black line at t = 24 hrs indicate time at which 1.2 μM KaiA (dark turquoise in (a), brown in (b)) or buffer (turquoise in (a), orange in (b)) was spiked. (c) Comparison of native-PAGE (blue hollow circles) and baseline subtracted fluorescence anisotropy (brown) in the time window t = 0 – 12 hrs.

Figure S14. Real-time cw-EPR data analysis of $N19C_{3IAP}$-KaiC binding in the 1X oscillator.

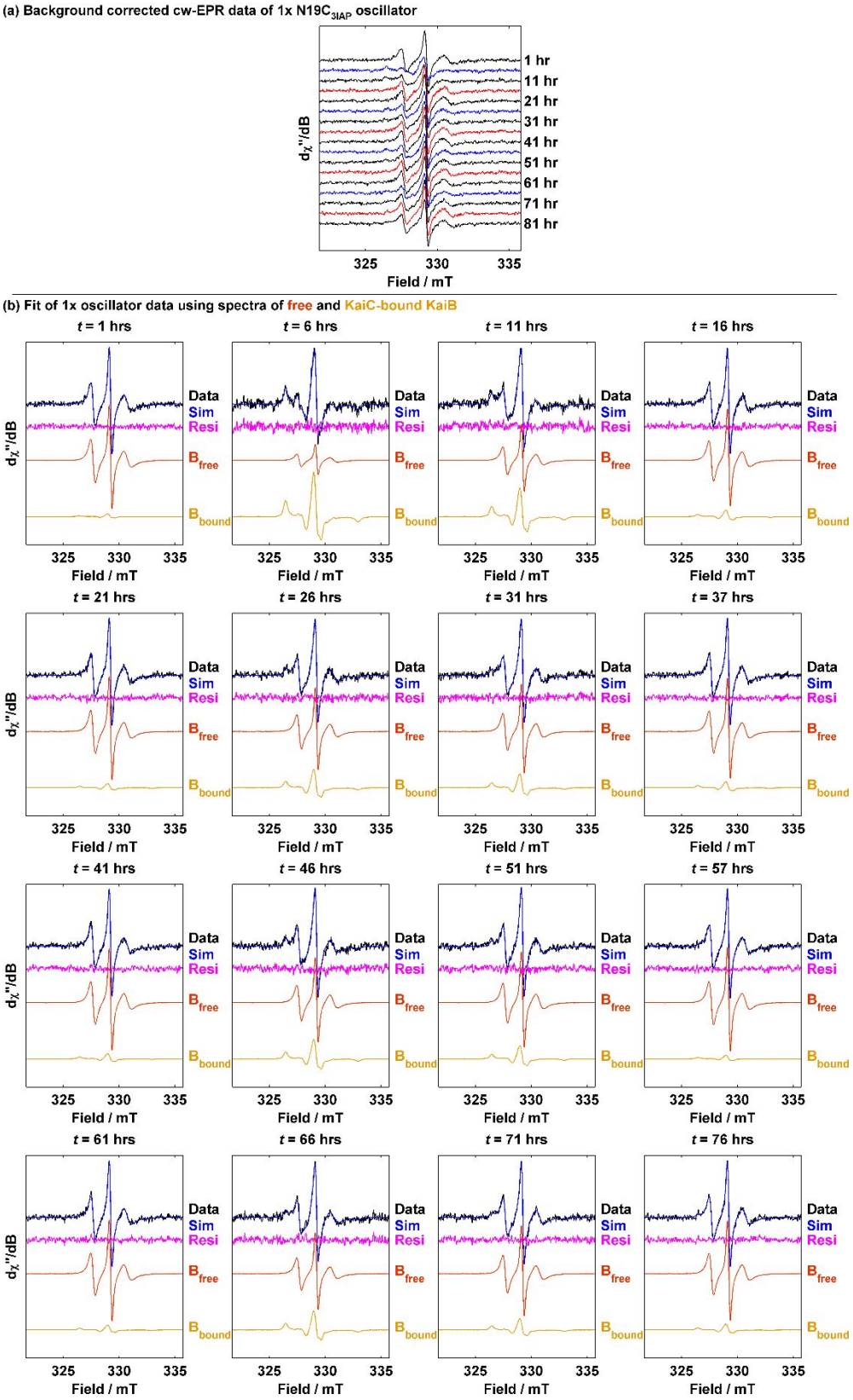

(a) Stacked plot of ~1-hour binned spectra (8 unbinned spectra). (b) Simulation of spectra at 5-hour intervals. Note that the times are not at regular 5-hour intervals due to slight deviation of spectral acquisition time from 7.5 minutes per spectrum.

Figure S15. Reproducibility of the 1X N19C$_{3IAP}$ oscillator.

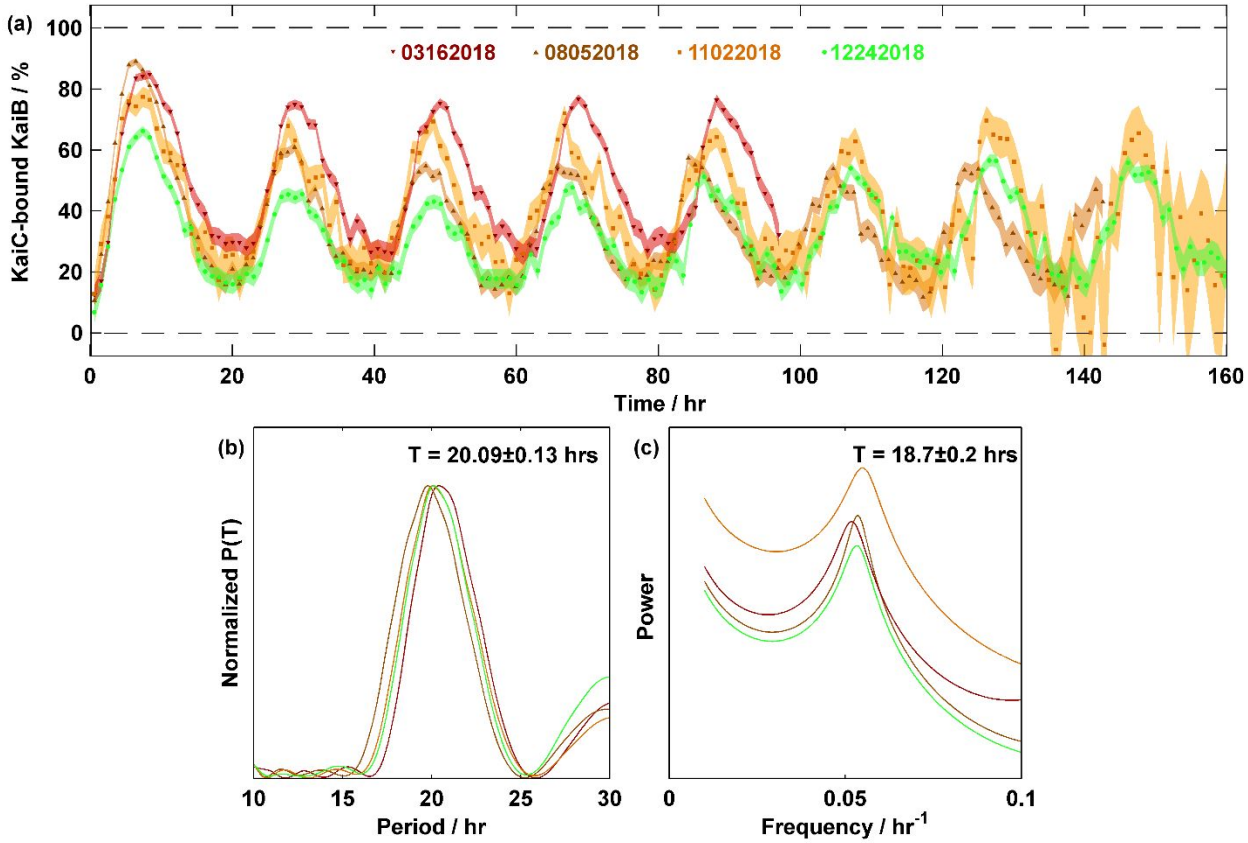

The 1X N19C$_{3IAP}$ oscillator was repeated 4 times in 4 different weeks. (a) cw-EPR derived kinetics of all trials. Trial 1 (dark red downward facing triangles), Trial 2 (brown upward facing triangles), Trial 3 (orange squares) and Trial 4 (light green circles). Data were binned by 1-hour bins. Shaded area shows 95% CI. (b) Lomb-Scargle periodogram. (c) Maximum entropy spectral analysis. For (b) and (c), the color schemes follow (a) whereas the periods are given in mean ± SEM format.

Figure S16. Phenomenological fitting of $N19C_{3IAP}$-KaiC binding with sum of cosines.

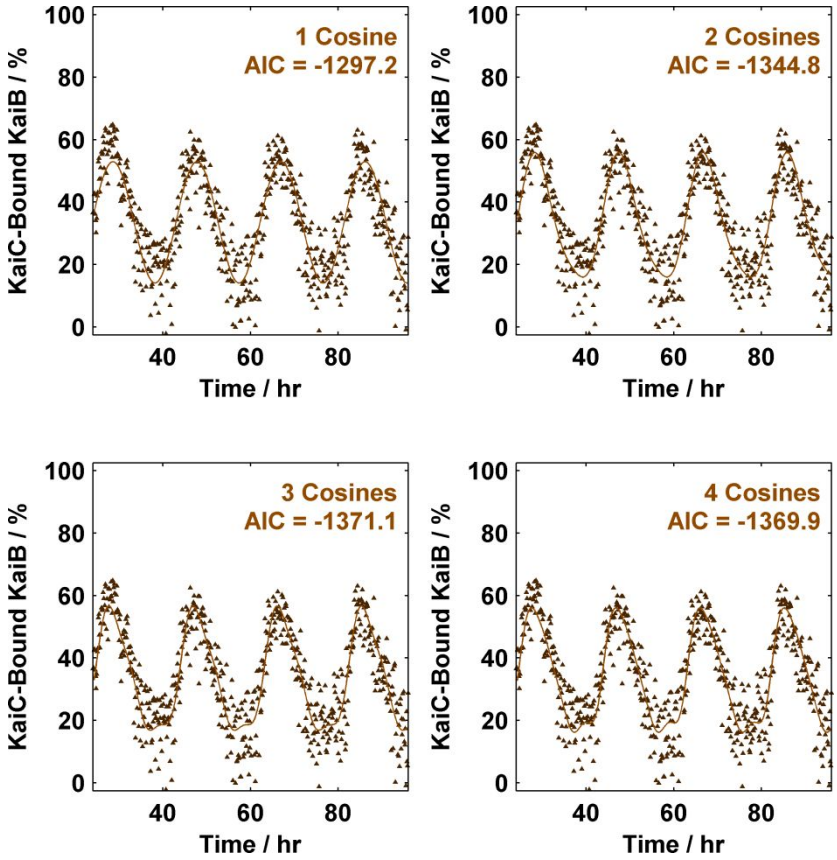

Upward facing triangles indicate cw-EPR based kinetics. Dash-dot line indicates fit to sum of cosines. The data shown is the same trial as Fig. 5, and Trial 2 in S15 and Table S5.

Table S5. mFourfit parameters of $N19C_{3IAP}$ 1X oscillator data.

$N19C_{3IAP}$ 1x oscillator mFourfit parameters for oscillation of fraction of KaiC-bound KaiB over time determined by nonlinear least squares for four independent trials. Parameters shown were determined from unbinned data between t = 24 – 97 hrs (~0.125 hour per point). Errors shown are 95% confidence interval (CI) via the Jacobian matrix.

Trial 1 (03162018, dark red downward facing triangles in Fig. S15)

q	1	2	3	4
C / %	48.3 ± 0.6	48.3 ± 0.6	48.3 ± 0.6	48.3 ± 0.6
T / hr	20.03 ± 0.11	20.04 ± 0.09	20.04 ± 0.08	20.04 ± 0.08
A_1 **/ %**	-23.7 ± 0.9	-23.6 ± 0.8	-23.5 ± 0.8	-23.5 ± 0.8
φ_1 **/ hr**	-0.38 ± 0.35	-0.35 ± 0.28	-0.36 ± 0.27	-0.36 ± 0.27
A_2 **/ %**	-	5.2 ± 0.8	5.3 ± 0.8	5.3 ± 0.8
φ_2 **/ hr**	-	-1.72 ± 0.34	-1.70 ± 0.33	-1.69 ± 0.33
A_3 **/ %**	-	-	1.7 ± 0.8	1.7 ± 0.8
φ_3 **/ hr**	-	-	0.50 ± 0.53	0.52 ± 0.53
A_4 **/ %**	-	-	-	-0.4 ± 0.8
φ_4 **/ hr**	-	-	-	-0.60 ± 1.64
$A_{peak\text{-}to\text{-}peak}$ **/ %**	47.4	50	48.7	48.1
RSS	3.63	2.83	2.74	2.74
p**(AIC)**	5	7	9	11
AIC	-1355.1	-1500.5	-1515.7	-1512.6

Trial 2 (08052018, brown upward facing triangles in Fig. S15, also in Fig. 5 and S14, S16)

q	1	2	3	4
C / %	33.5 ± 0.7	33.4 ± 0.6	33.3 ± 0.6	33.3 ± 0.6
T / hr	19.20 ± 0.14	19.21 ± 0.12	19.23 ± 0.11	19.22 ± 0.11
A_1 **/ %**	-19.4 ± 0.9	-19.5 ± 0.9	-19.5 ± 0.9	-19.5 ± 0.9
φ_1 **/ hr**	-0.21 ± 0.46	-0.21 ± 0.41	-0.25 ± 0.37	-0.24 ± 0.37
A_2 **/ %**	-	3.3 ± 0.9	3.4 ± 0.9	3.5 ± 0.9
φ_2 **/ hr**	-	-1.09 ± 0.54	-1.11 ± 0.49	-1.09 ± 0.49
A_3 **/ %**	-	-	2.5 ± 0.9	2.5 ± 0.9
φ_3 **/ hr**	-	-	0.99 ± 0.48	1.00 ± 0.48
A_4 **/ %**	-	-	-	-0.7 ± 0.9
φ_4 **/ hr**	-	-	-	-0.86 ± 0.97
$A_{peak\text{-}to\text{-}peak}$ **/ %**	38.8	39.9	39.8	39.8
RSS	4	3.67	3.49	3.47
p**(AIC)**	5	7	9	11
AIC	-1297.2	-1344.8	-1371.1	-1369.9

Trial 3 (11022018, orange squares in Fig. S15)

q	1	2	3	4
C / %	36.3 ± 1.3	36.1 ± 1.3	36.1 ± 1.3	36.1 ± 1.3
T / hr	19.67 ± 0.25	19.62 ± 0.23	19.61 ± 0.22	19.62 ± 0.22
A_1 **/ %**	-22.2 ± 1.9	-22.4 ± 1.8	-22.3 ± 1.8	-22.4 ± 1.8
φ_1 **/ hr**	-0.76 ± 0.81	-0.56 ± 0.74	-0.53 ± 0.73	-0.56 ± 0.72
A_2 **/ %**	-	4.2 ± 1.8	4.2 ± 1.8	4.2 ± 1.8
φ_2 **/ hr**	-	-12.07 ± 1.03	-12.02 ± 1.01	-12.07 ± 1.01
A_3 **/ %**	-	-	1.0 ± 1.8	0.9 ± 1.8
φ_3 **/ hr**	-	-	0.96 ± 1.93	1.00 ± 2.09
A_4 **/ %**	-	-	-	-1.2 ± 1.8
φ_4 **/ hr**	-	-	-	0.81 ± 1.31
$A_{\text{peak-to-peak}}$ **/ %**	44.4	47.1	46.7	49.2
RSS	15.9	15.4	15.4	15.3
p**(AIC)**	5	7	9	11
AIC	-465.61	-481.7	-478.91	-476.73

Trial 4 (12242018, light green circles in Fig. S15)

q	1	2	3	4
C / %	28.8 ± 0.7	28.7 ± 0.6	28.7 ± 0.6	28.7 ± 0.6
T / hr	19.70 ± 0.18	19.68 ± 0.16	19.68 ± 0.16	19.69 ± 0.15
A_1 **/ %**	-15.1 ± 0.9	-15.1 ± 0.9	-15.0 ± 0.9	-15.0 ± 0.9
φ_1 **/ hr**	-0.64 ± 0.60	-0.54 ± 0.54	-0.55 ± 0.52	-0.57 ± 0.50
A_2 **/ %**	-	2.6 ± 0.9	2.6 ± 0.9	2.6 ± 0.9
φ_2 **/ hr**	-	-1.26 ± 0.71	-1.22 ± 0.69	-1.24 ± 0.69
A_3 **/ %**	-	-	1.0 ± 0.9	1.0 ± 0.9
φ_3 **/ hr**	-	-	1.06 ± 1.01	1.11 ± 0.98
A_4 **/ %**	-	-	-	-1.1 ± 0.9
φ_4 **/ hr**	-	-	-	-0.11 ± 0.78
$A_{\text{peak-to-peak}}$ **/ %**	30.1	30.6	30.5	31.6
RSS	3.96	3.77	3.74	3.7
p**(AIC)**	5	7	9	11
AIC	-1302.4	-1329	-1330	-1331.7

SUPPLEMENTARY TEXT

Maximum error of frequency correction

In the methods section, two methods of frequency correction via multiplication of frequency ratio (eq. 1b) or addition by frequency difference (eq. 1c) were discussed and implemented. In both cases, because the magnetic field sweep window B_w is fixed by the settings used at t = 0 hrs with 1024 field points spanning 200 G, direct comparison between a spectrum collected at e.g. 9.2400 GHz $y_0(B_w)$ and 9.2405 GHz with the latter with corrected field positions $y_1(B_{w'})$ is not possible because their x-abscissa are different. This is solved by interpolating the frequency corrected spectrum to the original magnetic field positions via MATLAB routine `interp1` to convert $y_1(B_{w'})$ to $y_1(B_w)$. The interpolation procedure produces NaNs on the edges of the spectra which are then converted to zeroes for further processing. We note here that replacing these values with zeroes do not interfere with data analysis as the nitroxide transitions span only about 100 G even in the near-rigid limit at X-band (Fig. S8a).

The merits and maximum error introduced by the frequency correction methods shall be revisited below by rewriting the correction equations.

(1) Frequency correction via frequency ratio

Microwave frequency drift correction can be implemented by multiplying the frequency ratios of two spectra collected at slightly different frequencies.

$$B_1 = \frac{h\nu_1 - AI}{g\mu_B} + \ldots = \left(\frac{h\nu_0 - AI}{g\mu_B}\right)\left(\frac{\nu_1}{\nu_0}\right) + \frac{AI}{g\mu_B}\left(\frac{\nu_1}{\nu_0} - 1\right) + \ldots \approx \frac{B_0\nu_1}{\nu_0} \ldots (S1a)$$

The error term ε_{1b} is hence

$$\varepsilon_{1b} = \frac{AI}{g\mu_B}\left(\frac{\nu_1}{\nu_0} - 1\right)$$

Worst case scenario is achieved when the largest component of A, A_z, is considered in the near-rigid limit with minimized g.

$$\varepsilon_{1b,max} = \frac{(100\ \text{MHz})(6.626 \times 10^{-34}\text{J}\cdot\text{s})(1)}{(2.0023)(9.274 \times 10^{-24}\text{J}\cdot\text{T}^{-1})}\left(\frac{9.2405\ \text{GHz}}{9.2400\ \text{GHz}} - 1\right) \approx 2 \times 10^{-7}\text{T} = 2 \times 10^{-4}\text{mT}$$

Hence, equation 1b produces a maximum error of 2×10^{-4} mT, 2 orders of magnitude smaller than the magnetic field intervals (2×10^{-2} mT).

(2) Frequency correction via linear shift

Microwave frequency drift correction can be implemented by shifting the magnetic field axis linearly.

$$B_1 = \frac{h\nu_1 - AI}{g\mu_B} + \ldots = \frac{h\nu_1 - h\nu_0 + h\nu_0 - AI}{g\mu_B} + \ldots = B_0 + \frac{h(\nu_1 - \nu_0)}{g\mu_B} \ldots (\text{S1}b)$$

The error in the field correction ε_{1c} stems from anisotropy of g.

$$\varepsilon_{1c} = \frac{h(\nu_1 - \nu_0)}{\mu_B}\left(\frac{1}{g} - \frac{1}{g_e}\right)$$

Worst case scenario is achieved with the most anisotropic g-value.

$$\varepsilon_{1c,max} = \frac{(6.626 \times 10^{-34}\text{J}\cdot\text{s})(0.5\ \text{MHz})}{9.274 \times 10^{-24}\text{J}\cdot\text{T}^{-1}}\left|\frac{1}{2.0082} - \frac{1}{2.0023}\right| \approx 5 \times 10^{-8}\text{T} = 5 \times 10^{-5}\text{mT}$$

Hence, equation 1c produces a maximum error of 5×10^{-5} mT, which is almost 3 orders of magnitude smaller than the magnetic field intervals.

Thus, both methods produce magnetic field correction errors that are significantly less than the magnetic field intervals of the spectra collected and can be considered negligible. We note that (1c) gives a smaller maximum error than (1b) for the nitroxide system at X-band whereas we opted to use (1b) throughout the manuscript. The above calculations justify the use of either methods.

Estimation of KaiB-KaiA direct binding dissociation constant.

In the main text, Fig. S9 and Table S4, we attempted to estimate the dissociation constant between KaiA and KaiB based on N19C$_{3IAP}$-KaiA data alone. We mentioned that subtraction-simulation based quantification produced a lower limit on the fraction of KaiA-bound KaiB. To prove this assertion, consider the reaction again:

$$A_2 + B \rightleftharpoons A_2B$$

We assume that free KaiB and A_2B each possesses their respective spectra B_{free} and B_{A_2B} such that the real-time cw-EPR data matrix Y can be written as

$$Y = Bw = \begin{pmatrix} B_{\text{free}} & B_{A_2B} \end{pmatrix} \begin{pmatrix} w_{\text{free}} \\ w_{A_2B} \end{pmatrix} \ldots (\text{S2})$$

where w refers to the weights of the components. It is theoretically possible that the spin label redistributes its rotamer populations on binding KaiA such that B_{A_2B} partially resembles B_{free}:

$$B_{A_2B} = (1 - \phi)B_{\text{free}} + \phi B_c \ldots (\text{S3}a)$$

where $0 \leq \phi \leq 1$ is a tunable parameter describing the distinctness of B_{A_2B} from B_{free} whereas B_c is some unknown spectrum. We can rewrite eq. S2 as

$$Y = \begin{pmatrix} B_{\text{free}} & (1 - \phi)B_{\text{free}} + \phi B_c \end{pmatrix} \begin{pmatrix} w_{\text{free}} \\ w_{A_2B} \end{pmatrix} \ldots (\text{S3}b)$$

Using a change-of-basis matrix R, we get

$$Y = BRR^{-1}w, R = \begin{pmatrix} 1 & -\dfrac{1-\phi}{\phi} \\ 0 & \dfrac{1}{\phi} \end{pmatrix}, R^{-1} = \begin{pmatrix} 1 & 1-\phi \\ 0 & \phi \end{pmatrix} \ldots (\text{S4}a)$$

$$Y = (B_{\text{free}} \quad B_c)\begin{pmatrix} w_{\text{free}} + (1-\phi)w_{A_2B} \\ \phi w_{A_2B} \end{pmatrix} \ldots (\text{S4}b)$$

At ϕ = 0, B_{free} and B_{A_2B} are indistinguishable. As ϕ increases, the two states become spectroscopically distinct but some of the population in A_2B is misattributed to the population of free KaiB. When ϕ approaches 1, the spectra of the two states are distinct and A_2B is no longer misattributed to free KaiB. This analysis implies that quantification is accurate only if we can find conditions such that ϕ = 1. Spectral subtraction analysis thus relies on the assumptions that

(1) B_c is well modelled by a typical nitroxide experiencing some motional dynamics and

(2) ϕ = 1.

The assumptions are bypassed when binding saturation conditions can be found as in the case of $N19C_{3IAP}$-$KaiC_{EE}$. However, this was not achieved with the KaiA-KaiB system. We observed from Fig. S9c that assumption (1) was fulfilled in that the difference spectrum between tenfold excess KaiA versus control could be well simulated with a nitroxide undergoing isotropic Brownian rotational motion. As there is insufficient data to test assumption (2) without further manipulating KaiB, we qualitatively examine the impact of $\phi < 1$. Specifically, eq. S4b implies that $\phi < 1$ leads to overestimation of w_{free} and underestimation of w_{A_2B} and hence $[A_2B]$. The downstream effect of the latter is that the apparent dissociation constant

$$K_D^{app} = \frac{[A_2][B]}{[A_2B]} = \frac{([A_2]_0 - [A_2B])([B]_0 - [A_2B])}{[A_2B]}$$

is an overestimate.

ACS ACS Publications C&EN CAS

Access provided by - Access paid by the | UC Merced Library | Log In

ACS Publications
Most Trusted. Most Cited. Most Read.

Search text, DOI, authors, etc.

My Activity Publications

COVID-19 Remote Access Support: Learn More about expanded access to ACS Publications research.

Most Read Articles

Description:

Most Read articles are refreshed daily and are based on full text downloads (PDF and HTML) from the previous 30 days and previous 12 months. Below are the journal's Top 20 most downloaded articles for the previous 30 days.

Biochemistry

1 month

12 Months

Improving the Treatment of Acute Lymphoblastic Leukemia

Ashish Radadiya, Wen Zhu, Adriana Coricello, Stefano Alcaro, and Nigel G. J. Richards*

Biochemistry 2020 59, 35, 3193-3200 **(Article)** ACS Editors' Choice
Publication Date (Web): August 12, 2020
ACS Editors' Choice Date: August 23, 2020

Abstract Full Text PDF

ABSTRACT

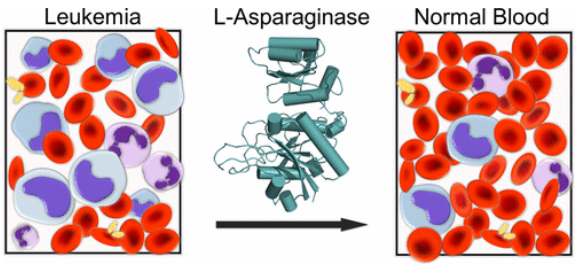

Monitoring Protein–Protein Interactions in the Cyanobacterial Circadian Clock in Real Time via Electron Paramagnetic Resonance Spectroscopy

Gary K. Chow, Archana G. Chavan, Joel C. Heisler, Yong-Gang Chang, Andy LiWang*, and R. David Britt*

Biochemistry 2020 59, 26, 2387-2400 **(Article)** ACS Editors' Choice
Publication Date (Web): May 26, 2020
ACS Editors' Choice Date: June 17, 2020

Abstract Full Text PDF

ABSTRACT

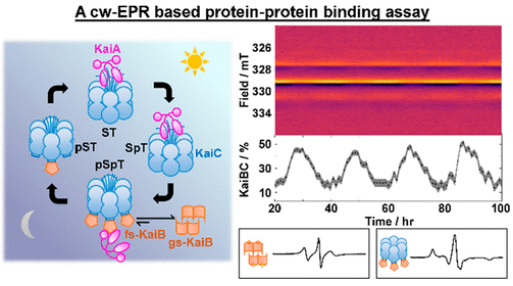

Tuning the Flexibility of Glycine-Serine Linkers To Allow

Rational Design of Multidomain Proteins

Martijn van Rosmalen, Mike Krom, and Maarten Merkx*

Biochemistry 2017 56, 50, 6565-6574 **(Article)** ACS AuthorChoice
Publication Date (Web): November 23, 2017

Abstract Full Text PDF

ABSTRACT

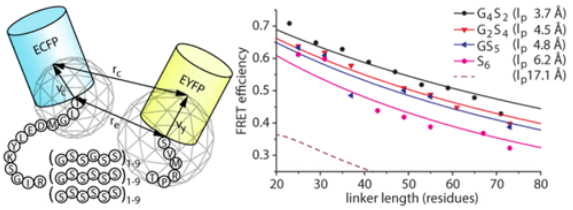

On the Temperature Dependence of Enzyme-Catalyzed Rates

Vickery L. Arcus*, Erica J. Prentice, Joanne K. Hobbs, Adrian J. Mulholland, Marc W. Van der Kamp, Christopher R. Pudney, Emily J. Parker, and Louis A. Schipper

Biochemistry 2016 55, 12, 1681-1688 **(Article)** ACS Editors' Choice
Publication Date (Web): February 16, 2016
ACS Editors' Choice Date: March 8, 2016

Abstract Full Text PDF

ABSTRACT

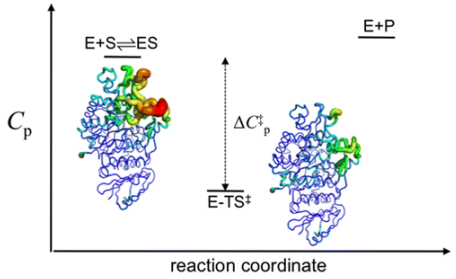

P-Bodies: Composition, Properties, and Functions

Yang Luo, Zhenkun Na, and Sarah A. Slavoff*

Biochemistry 2018 57, 17, 2424-2431 **(Article)** ACS AuthorChoice
Publication Date (Web): January 30, 2018

Abstract Full Text PDF

ABSTRACT

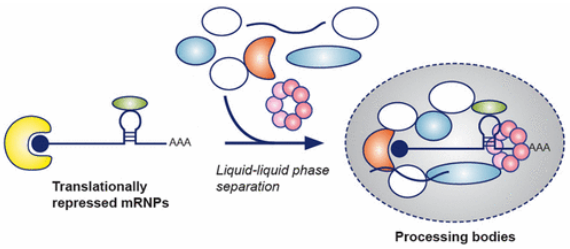

Yeast Alcohol Dehydrogenase Structure and Catalysis

Savarimuthu Baskar Raj, S. Ramaswamy, and Bryce V. Plapp*

Biochemistry 2014 53, 36, 5791-5803 **(Article)** ACS AuthorChoice
Publication Date (Web): August 26, 2014

Abstract Full Text PDF

ABSTRACT